Mon. Not. R. Astron. Soc. **000**, 000–000 (0000) Printed 6 February 2015 (MN LATEX style file v2.2)

New OB star candidates in the Carina Arm around Westerlund 2 from VPHAS+

M. Mohr-Smith,[1⋆] J. E. Drew,[1] G. Barentsen,[1] N. J. Wright,[1] R. Napiwotzki,[1] R. L. M. Corradi,[2] J. Eislöffel,[3] P. Groot,[3] V. Kalari,[4] Q. A. Parker,[5,6,7] R. Raddi,[8] S. E. Sale,[9] Y. C. Unruh,[10] J. S. Vink,[4] and R. Wesson [11]

[1] *Centre for Astrophysics Research, Science and Technology Research Institute, University of Hertfordshire, Hatfield AL10 9AB, UK*
[2] *Instituto de Astrofisica de Canarias, E-38200 La Laguna, Tenerife, Spain*
[3] *Afdeling Sterrenkunde, Radboud Universiteit Nijmegen, Faculteit NWI, Postbus 9010, NL-6500 GL Nijmegen, the Netherlands*
[4] *Armagh Observatory, College Hill, Armagh, BT61 9DG, UK*
[5] *Department of Physics & Astronomy, Macquarie University, Sydney, NSW 2109 Australia*
[6] *Research Centre for Astronomy, Astrophysics and Astrophotonics, Macquarie University, Sydney, NSW 2109 Australia*
[7] *Australian Astronomical Observatory, PO Box 296, Epping, NSW 1710, Australia*
[8] *Department of Physics, University of Warwick, Gibbet Hill Road, Coventry CV4 7AL, UK*
[9] *Rudolf Peierls Centre for Theoretical Physics, Keble Road, Oxford OX1 3NP, UK*
[10] *Department of Physics, Blackett Laboratory, Imperial College London, Prince Consort Road, London, SW7 2AZ, UK*
[11] *European Southern Observatory, Alonso de Cordova 3107, Casilla 19001, Santiago, Chile*

6 February 2015

ABSTRACT

O and early B stars are at the apex of galactic ecology, but in the Milky Way, only a minority of them may yet have been identified. We present the results of a pilot study to select and parametrise OB star candidates in the Southern Galactic plane, based on new data from the VPHAS+ survey. A 2 square-degree field capturing the Carina Arm around the young massive star cluster, Westerlund 2, is examined. The confirmed OB stars in this cluster are used to validate our identification method, based on selection from the $(u-g, g-r)$ diagram for the region. Our Markov Chain Monte Carlo fitting method combines VPHAS+ u, g, r, i with published J, H, K photometry in order to derive posterior probability distributions of the stellar parameters $\log(\mathrm{T_{eff}})$ and distance modulus, together with the reddening parameters A_0 and R_V. The stellar parameters are sufficient to confirm OB status while the reddening parameters are determined to a precision of $\sigma(A_0) \sim 0.09$ and $\sigma(R_V) \sim 0.08$. There are 356 objects selected as new OB candidates (earlier than ∼B2) with 37 emerging as new candidate O stars and 5 as new blue supergiant candidates. Most of the new objects are likely to be at distances between 3 and 6 kpc. We have confirmed the results of previous studies that these sight lines, at these longer distances, require non-standard reddening laws with $3.5 < R_V < 4$. In the outskirts of Westerlund 2, 1–2 arcmin north and south of the cluster centre, there is evidence of a potentially systematic rise in R_V to > 4.

Key words: stars: early-type, (Galaxy:) open clusters and associations: individual: Westerlund 2, (ISM:) dust, extinction, Galaxy: structure, surveys

1 INTRODUCTION

Stars of spectral type O and early B, more massive than $\sim 8M_{\odot}$, are massive enough to form collapsing cores at the end of their nuclear-burning lifetimes (see e.g. Langer 2012; Smartt 2009). It is widely recognised that these stars - hence-forward OB stars - are an important source of kinetic energy, driving turbulence and mixing of the interstellar medium, powered by a range of phenomena (stellar winds, wind-blown bubbles, expanding HII regions and supernova explosions). They are the main source of ultra-violet radiation in galaxies and, being short-lived ($\lesssim 40$ Myr), they are excellent tracers of recent star formation.

⋆ E-mail: m.smith10@herts.ac.uk

© 0000 RAS

In the Galaxy, clusters containing OB stars and OB associations have played an important role in tracing spiral arm structure (e.g. Russeil 2003; Vallée 2008). The typical scale height estimated for OB stars, forming in the Galactic disk, is a few 10s of pc (e.g. Reed 2000; Garmany et al. 1982), in keeping with estimates of the scale height for giant molecular clouds, their birth sites (e.g. Stark & Lee 2005). Being short-lived, OB stars are usually regarded as favouring clustered environments and as less common in the field. Occasionally however, examples of isolated field O stars are found and the question arises as to whether these high-mass star have formed in situ or have been ejected as runaways (see e.g. Portegies Zwart et al. 2010; Bestenlehner et al. 2011). In the Milky Way $\sim 96\%$ of known O-type stars have been identified as members of young open clusters, OB associations or as otherwise kinematically linked to clustered environments (de Wit et al. 2005). The present census leaves up to $\sim 4\%$ of Galactic O-type stars possibly forming in isolation, perhaps as the result of stochastic sampling of the initial mass function (IMF) as outlined by Parker & Goodwin (2007). Deep comprehensive searches for OB stars away from clusters have not been undertaken hitherto.

As luminous objects detected to great distances across the Galactic disk and through substantial obscuration, OB stars have long been recognised as a highly-suitable means for characterising the spatial variation of interstellar extinction, in terms of both dust column and extinction law (e.g. Cardelli et al. 1989; Fitzpatrick & Massa 2007). This is aided by their relatively simple optical near-infrared (OnIR) spectral energy distributions (SEDs). It follows from this that the more densely we can map the positions and extinctions towards these luminous probes, the more high-quality empirical constraints we can set on the 3-D distribution of dust and dust properties across the Galactic Plane.

Both of the above areas of enquiry will be well served by a deeper, more comprehensive mapping of the OB stars in the Milky Way. Past cataloguing efforts have been limited to brighter, nearer objects (e.g Garmany et al. 1982; Reed 2003; Maíz-Apellániz et al. 2004). Indeed the most comprehensive collection so far, 'The Catalog of Galactic OB Stars' (Reed 2003) contains ~ 16000 known or suspected OB stars taken from across the literature: around 95% of the entries are brighter than $13^{\rm th}$ magnitude in the visual bands. Now is the right time to push the magnitude limit much fainter, to $\sim 20^{\rm th}$ magnitude, given the likely delivery of astrometry to this depth by the Gaia mission from ~ 2017 onwards (both parallaxes *and* proper motions, for details on expected performance see de Bruijne 2012). Efficient, purely photometric selection of OB stars in the field as well as in clusters continues to be best undertaken at blue optical wavelengths, where colour selection via the Q method (initiated by Johnson & Morgan 1953a) is proven to separate O and early B stars from later type stars.

The practical motivation of this paper is to establish a method of photometric selection and analysis that can form the basis for a new homogeneous census of Galactic OB stars as faint as $g \simeq 20$. Based on a restrained extrapolation of the first results presented here, we can surmise that a new census will more than double the numbers known. A suitable source for the new census will be the VST Photometric Hα Survey of the Southern Galactic Plane and Bulge (VPHAS+ Drew et al. 2014). VPHAS+ is a deep, uniform, photometric survey of the entire southern Galactic Plane and Bulge in broad-band u, g, r, i and narrow-band Hα filters on ESO's VLT Survey Telescope (VST). The survey footprint includes the entire southern Galactic Plane within the Galactic latitude range of $|b| < 5^\circ$. The VST's OmegaCam imager provides a full square degree field of view with very good spatial resolution (0.2" pixels sample a median seeing of 0.8 – 1.0 arcsec in the $u/g/r$ bands).

Here, we present a first study that uses broadband VPHAS+ data to select and parametrize OB stars in a 2 square-degree area, roughly centred on $\ell = 284^\circ$, $b = -0.7^\circ$, in the part of the Plane containing the young massive cluster, Westerlund 2 (Wd 2), the larger associated HII region RCW 49, and the diffuse nebula NGC3199 (see Figure 1). Previous optical and near-infrared studies on the stellar content of Westerlund 2 have focused on the immediate environment of the cluster itself - a patch of sky 4 arcmin across - (Moffat et al. 1991; Ascenso et al. 2007; Vargas Álvarez et al. 2013), while the x-ray study by Tsujimoto et al. (2007) focused on an area ~ 17 arcmin across. Most recently, Hur et al. (2015) have revisited optical photometry of this cluster over a 17.9' x 9.3' footprint.

By tracing 8μm warm-dust emission Rahman & Murray (2010) have identified this same region as part of a large star-forming complex (G283). On the sky, Wd 2 falls close to the Carina Arm tangent direction (e.g. Russeil 2003): the CO data presented by Dame (2007) show persuasively that Wd 2 and its environs fall just inside the sky position of the tangent point, but further away. This cluster is estimated to be 1 - 3Myr old. It contains a large number of spectroscopically-confirmed OB stars, albeit behind a dust column giving rise to over 6 magnitudes of visual extinction (Moffat et al. 1991; Rauw et al. 2007; Carraro et al. 2012; Vargas Álvarez et al. 2013). Estimates of the distance to Wd 2 in the literature have varied enormously, ranging from 2.8 kpc (Ascenso et al. 2007) up to ∼8 kpc (e.g. Rauw et al. 2011). However, it is not our aim to enter into this debate. More important is the likelihood that much of the scientific gain from VPHAS+ discoveries of OB stars will be in the domain of visual extinctions of up to 8–10 magnitudes, and distance scales of 2–10 kpc (according to Galactic longitude). In this regard, the field around Wd 2 is highly typical of the task ahead.

A recent study on Wd 2 by Vargas Álvarez et al. (2013) uses data from the Hubble Space Telescope (HST) that offers much better spatial resolution than is achievable from the ground. This is the only dataset that offers better angular resolution than the new VPHAS+ data analysed here. These authors' values of R_V and A_V were derived by fitting, to 32 individual OB stars in or near Wd 2, reddened model optical/near-infrared SEDs appropriate for the selected stars' spectroscopically-confirmed spectral types. The best fits were computed by seeking the global chi-squared minimum among all plausible values of R_V and A_V – resulting in a mean outcome of $R_V = 3.77 \pm 0.09$ and $A_V = 6.51 \pm 0.38$ mag combining results from different reddening law prescriptions. We use a comparison of our OnIR SED fit results for this same set of OB stars to bench-mark our method.

This paper is organised as follows. In Section 2 more details on the data used for this study are given. Section 3 is a presentation of our method, beginning with the updated

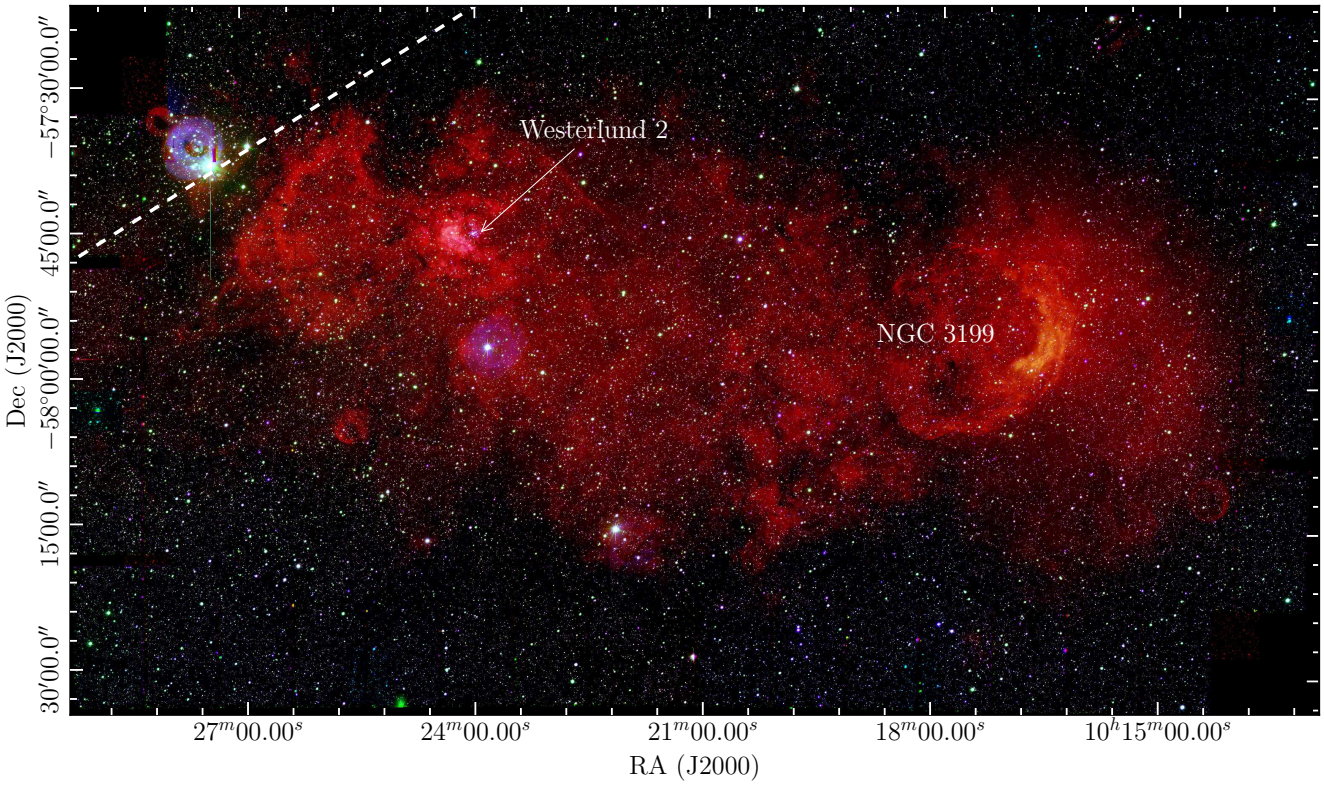

Figure 1. RGB image of the ∼2 square degree region (Hα, g, i). This region falls within the star forming complex G283 identified by Rahman & Murray (2010) – an elliptical region slightly larger than the sky area shown. Westerlund 2 is embedded in the HII region RCW49, while the diffuse nebulae NGC3199 is located to the right (West) as marked. The dashed line traces the Galactic equator.

version of the Q method of OB star selection that we use, and ending with a description of the Markov Chain Monte Carlo (MCMC) sampling of the posterior distributions of the OnIR SED model fit parameters. The stage is then set to compare our results for Wd 2 stars with those of Vargas Álvarez et al. (2013), in Section 4. The results of the fits to the final list of 356 new OB candidates drawn from across the full 2 square degrees are presented in Section 5. This is followed by a discussion of the results in Section 6, in which we consider the extinction trends revealed in this region, and draw attention to the newly discovered O stars outside the confines of Wd 2. The outlook and our conclusions are summarised in Section 7.

2 THE DATA

We make use of the photometry from two VPHAS+ fields, numbered 1678 and 1679, that are respectively centred on RA 10 18 10.91, Dec -58 03 52.3 (J2000) and on RA 10 25 27.27, Dec -58 03 52.3 (J2000). These were observed in succession in the u, g and r filters on the night of 22$^{\rm nd}$ January 2012. The red filter data in Hα, r and i were obtained on 29$^{\rm th}$ April 2012. The seeing, as measured from the data point spread function, was variable on the earlier night ranging from 0.62 at best in g up to 1.24 at worst in r. When the exposures in the red filters were obtained 3 months later, conditions were more stable, with the typical seeing ranging from 0.8 to 1.0 arcsec. Viewed in comparison to all the VPHAS+ data collected so far, these observations rank as 2$^{\rm nd}$-quartile quality in u and g (i.e. relatively high quality), and 3$^{\rm rd}$-quartile in r, i and Hα. The 5σ magnitude limits on the single exposures are u: 21.0, g: 22.4, r: 21.5, i: 20.6, and Hα: 20.4. All magnitudes are in the Vega system. Full details on the survey strategy, the offsets, the exposure times, photometric quality and the data-processing pipeline used are given by Drew et al. (2014).

Our analysis begins with band-merged catalogues created from the single-band catalogues emerging from the CASU pipeline. In order to correct for the uncertainty in the initial calibration of VPHAS+, a comparison has been made with empirical g, r and i observations from the APASS survey and with synthetic tracks in the $(u-g, g-r)$ plane. The median difference between g, r and i in the two surveys was applied to the VPHAS+ data. The u band was then calibrated by applying an offset to the $u-g$ scale such that the number density of stars between the synthetic G0V reddening track and the unreddened main sequence is maximised. This ensures that the top and bottom edge of the main stellar locus are aligned with the synthetic tracks as shown in Figure 2. This resulted in offsets relative to the pipeline reduction of u: -0.35, g: 0.05, r: 0.01 and i: 0.05 for field 1678 and u: -0.34, g: 0.06, r: 0.01 and i: 0.01 for field 1679. With an improved calibration in place, we select stars in the magnitude range $13 < g < 20$ and require random photometric errors to be less than 0.1. Mean magnitudes were taken when repeat photometry was available from the offset fields.

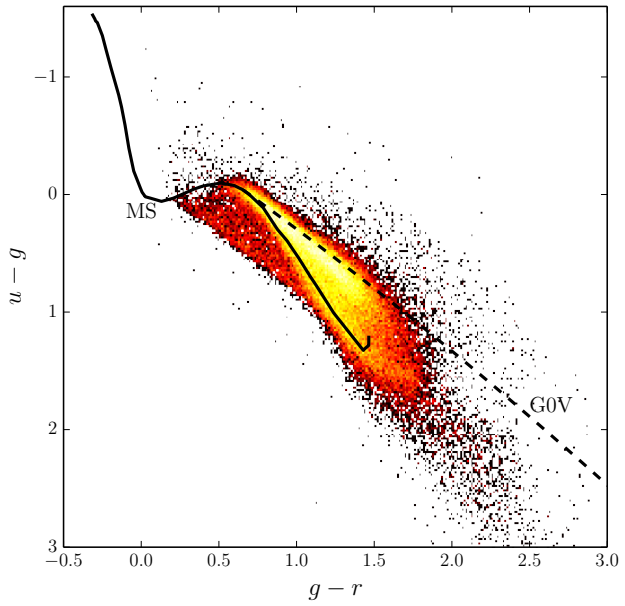

Figure 2. Calibration of VPHAS+ data with respect to synthetic reddening tracks from Drew et al. (2014). Both the main sequence and G0V reddening vector line up with the main stellar locus.

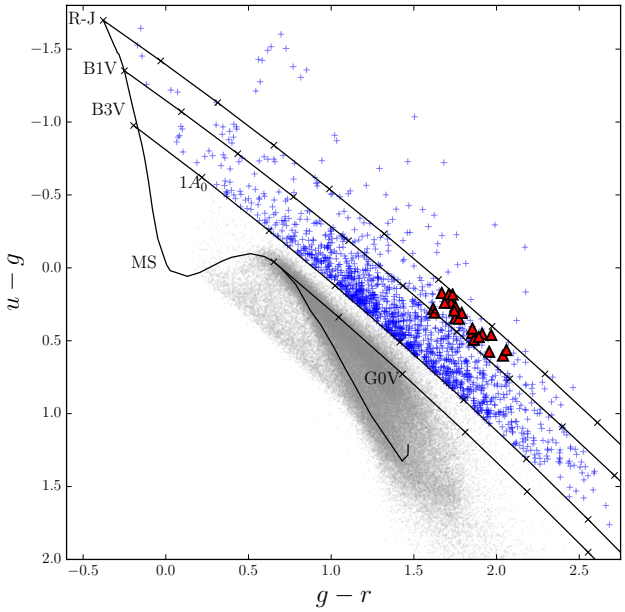

Figure 3. Selection of OB stars in and around Wd2. The lower reddening curve is that of a B3V, dropped by 0.1 in u-g in order to capture all early type B stars, and is characterised by an $R_V = 3.1$ law. The other reddening curves are that of a B1V and an ideal Rayleigh-Jeans spectrum and are characterised by an $R_V = 3.8$ law. Selected OB candidates are blue crosses while the known objects from Vargas Álvarez et al. (2013) are red triangles.

3 SELECTION AND FITTING METHOD

3.1 Photometric selection and cross matching

We select OB stars using a method that has its origins in the Q Method of Johnson & Morgan (1953b). On the $(u-g, g-r)$ diagram reddened OB stars of spectral type earlier than B3 are located above the main stellar locus. In principle no star can be bluer than the Rayleigh-Jeans (RJ) limit which sets an upper bound on the likely location of OB stars in the diagram. We select our candidate objects between the reddening lines associated with these two limiting types. Figure 3 shows the selection of OB candidates (blue crosses) across the two fields as well as the known OB stars from Vargas Álvarez et al. (2013) that were successfully cross matched with VPHAS+ (shown as red triangles). Over-plotted are the reddening tracks of a B3V, a B1V and that of a pure RJ spectrum all taken from Drew et al. (2014). The tracks we use take into account the measured red leak associated with the u-band filter.

Previous results from Carraro et al. (2012) and Vargas Álvarez et al. (2013) suggest an $R_V = 3.8$ reddening law is required towards Wd 2. The B1V and RJ reddening vectors have been drawn using this law. To avoid a bias towards this non-standard reddening law we have used the B3V $R_V = 3.1$ reddening vector as our lower selection limit and have dropped its position by 0.1 mags in $u-g$ in order to capture any early B stars that may have been missed. The lower the value of R_V, the steeper the reddening vector will be.

Each object was then cross matched to within $1''$ of the best available near infra-red detection in order to access J, H, K photometry. The mean angular cross-match distance was 0.09". As the stellar density in the central $\sim 4'$ of Wd 2 is very high, the Ascenso et al. (2007) NIR catalogue was the preferred partner on account of its superior angular resolution. Everywhere else 2MASS was used. This follows the approach taken by Vargas Álvarez et al. (2013).

3.2 SED fitting

We calculate the probability distribution of a range of model parameters corresponding to a set of empirical measurements, in a Bayesian scheme. This approach is chosen over a straight forward χ^2 minimisation scheme so that we may recover the full posterior probability distribution. This can reveal covariance between different parameters.

Given a set of empirical data, $d = \{d_1, .., d_i\}$, and a model, parametrised by a set of parameters, $\theta = \{\theta_1, .., \theta_i\}$, the *posterior* probability of the parameters can be calculated using Bayes' Theorem:

$$P(\theta \mid d) = \frac{P(d \mid \theta) \cdot P(\theta)}{P(d)} \quad (1)$$

In this expression, $P(d \mid \theta)$, the *likelihood* is the probability of the data being measured given a set of model parameters. The *posterior* and the *likelihood* are related by the *prior*, $P(\theta)$, which encodes any known constraints on the model parameters, including known physical bounds. Here $P(d)$ can be treated as a normalising constant and ignored. Hence the *posterior* probability distribution can be found by the relation:

$$P(\theta \mid d) \propto P(d \mid \theta) \cdot P(\theta) \quad (2)$$

In this work the empirical data are derived from the

Table 1. Sample values of the intrinsic SEDs with approximate spectral type equivalents. Magnitudes are in the Vega system.

ST	$\log(T_{\rm eff})$	u	g	r	i	J	H	Ks
O3V	4.65	-7.32	-5.78	-5.48	-5.33	-4.88	-4.73	-4.63
O9V	4.50	-5.28	-3.86	-3.60	-3.45	-3.03	-2.90	-2.80
B1V	4.40	-3.97	-2.70	-2.47	-2.34	-1.98	-1.85	-1.77
B3V	4.27	-2.31	-1.33	-1.16	-1.07	-0.80	-0.70	-0.65

observed SED of each star and they consist of optical and near infrared apparent magnitudes:

$$SED_{obs} = \{u, g, r, i, J, H, K_S\}, \tag{3}$$

and their uncertainties:

$$\sigma(SED_{obs}) = \{\sigma_u, \sigma_g, \sigma_r, \sigma_i, \sigma_J, \sigma_H, \sigma_{K_S}\}. \tag{4}$$

Along with the random flux errors supplied by the surveys, we have included a systematic uncertainty to account for the independent absolute calibration errors in each band. The values adopted for the latter are 0.04 in the u band, 0.03 in g, r and i, 0.03 in the J band and 0.02 in H and K_s (see Drew et al. 2014; Skrutskie et al. 2006).

The model parameters that we are interested in estimating are:

$$\theta = \{\log(\mathrm{T_{eff}}), \mathrm{A_0}, \mathrm{R_V}, \mu\} \tag{5}$$

Where $\log(\mathrm{T_{eff}})$ is the effective temperature, A_0 is the monochromatic extinction at 4595Å, R_V is the ratio of total to selective extinction and μ is the distance modulus.

3.2.1 Likelihood function

Defining the likelihood function requires us to define a forward model $SED_{mod}(\theta)$, which predicts the apparent SED of OB stars based on the model parameters θ. The intrinsic SEDs used in the model are taken from the Padova isochrone database (CMD v2.2 [1]; Bressan et al. 2012; Bertelli et al. 1994) and are supplied in the Vega system. The optical/NIR colours of OB stars do not vary significantly with luminosity class (Martins et al. 2005). Therefore $\log(g)$ was fixed and only main-sequence models were used ($\log(g) \sim 4.0$). Solar metallicity $Z = 0.019$ has been adopted throughout, in view of the fact that the sight lines we explore do not sample a wide range of Galactic radii. This is the same value as used by Vargas Álvarez et al. (2013). Fixing these parameters provides a simple grid of absolute magnitude, M_λ, as a function of $\log(\mathrm{T_{eff}})$ in each of the seven bands.

To obtain a continuous grid, each $M_\lambda - \log(\mathrm{T_{eff}})$ relationship was fit with a 2^{nd} order polynomial. It can be noted that a linear fit was also trialled but failed to characterize the distributions especially for the low-end values of $\log(\mathrm{T_{eff}})$. Table 1 provides sample SEDs.

The SEDs are then reddened using a Fitzpatrick & Massa (2007) reddening law, parametrised by A_0 and R_V, and then shifted according to a distance modulus. The apparent OnIR SEDs of O and early B stars are largely controlled by these quantities. This is because the OnIR intrinsic colours of OB stars change very slowly as a function of effective temperature (Martins et al. 2005), as the Rayleigh-Jeans limit is approached. This means that $\log(\mathrm{T_{eff}})$ is only weakly constrained, albeit well enough to reach our goal of confirming OB status. As we have no handle on luminosity class, the distance modulus takes the role of a normalisation factor and will also be weakly constrained. In contrast A_0 and R_V are very informative and well constrained.

We can now use the forward model to construct a *likelihood* model $P(SED_{obs} \mid \theta)$ that computes the probability of SED_{obs} given the set of physical parameters θ. Assuming that the uncertainties on the measurements are normally distributed and uncorrelated, this can be described by a multi-variate Gaussian:

$$P(SED_{obs} \mid \theta) \propto \exp\left[-\frac{1}{2}\left(SED_{obs} - SED_{mod}\right)^T \Sigma^{-1} \left(SED_{obs} - SED_{mod}\right)\right] \tag{6}$$

Where Σ is the covariance matrix containing the variance $\sigma^2(SED_{obs})$ in the leading diagonal. In this case Equation 6 reduces to the familiar sum for χ^2:

$$P(SED_{obs} \mid \theta) \propto \exp\left(-\frac{1}{2}\sum_i^n \frac{(m(obs)_i - m(mod)_i)^2}{\sigma_i^2}\right) \tag{7}$$

Where $m(obs)_i$ and $m(mod)_i$ are the observed and model magnitudes in each band i.

3.2.2 Priors

We adopt a uniform *prior* on each of the model parameters:

$$P(\theta) = \begin{cases} 1 \quad \text{if} \begin{cases} 4.2 \leqslant \log(\mathrm{T_{eff}}) \leqslant 4.7 \\ 0 \leqslant A_0 \leqslant 10 \\ 2.1 \leqslant R_V \leqslant 5.1 \\ 0 \leqslant \mu \leqslant 16 \end{cases} \\ 0 \quad \text{else} \end{cases} \tag{8}$$

The upper bound on $\log(\mathrm{T_{eff}})$ is governed by the available models and the lower bound is the typical temperature of a B3V star (Zorec & Briot 1991) in accordance with our selection in the $(u-g, g-r)$ diagram. The upper limit on A_0 is a plausible upper bound for detection of OB stars in VPHAS+ down to $g = 20$, assuming a typical rise in visual extinction of 1 magnitude per kpc. The constraints on R_V are the upper and lower limits measured in the Galaxy (Fitzpatrick & Massa 2007). Since we expect to find these objects at distances ranging between 3 and 10kpc, an upper limit on the distance modulus μ of 16 is sufficient to capture them all.

3.2.3 Sampling the posterior distribution using MCMC

Characterising the *posterior* distribution by computing the probability at all values in the parameter space is computationally expensive. Instead one can sample the distribution using a Markov Chain Monte Carlo (MCMC) algorithm.

[1] http://stev.oapd.inaf.it/cgi-bin/cmd

In this study we use the Python package *emcee* developed by Foreman-Mackey et al. (2013). In brief, the software takes a set of parameters and supplies them to a group of *n walkers*. The *walkers* then use a pseudo-random walk to sample the parameter space. At each sample the probability is calculated. By communicating their relative probabilities to one another the *walkers* are able to quickly find and sample the region of high probability without wasting computational time on the parameter combinations of very low probability. The software then returns what are known as *chains* which contain the values of the parameters at every step in the walk. The frequency at which each region in the parameter space is visited is proportional to its probability. The finer details can be found in Foreman-Mackey et al. (2013).

4 VALIDATION OF METHOD

First it is appropriate to verify that our selection method recovers known objects. Second we verify that the fitting algorithm delivers the expected results. To achieve this, we have chosen to compare with the results of the recent study by Vargas Álvarez et al. (2013). This is an informative comparison to make both because this study benefited from the superior angular resolution of HST and because Vargas Álvarez et al. (2013) used a combination of optical and NIR photometry to derive stellar reddenings as we do here.

4.1 Photometric selection

Vargas Álvarez et al. (2013) derived the extinction properties of 29 known OB stars in the central region of Wd 2, of which, 24 were successfully cross matched with VPHAS+ to within 1". Using the nomenclature from Vargas Álvarez et al. (2013), the five missing objects are #597, #826, #843, #903 and #906. They appear in some of the most crowded regions of the cluster: the angular resolution of VPHAS+ compared to that of HST is insufficient to separate them from brighter neighbours. Figure 4 shows the positions of the 24 cross-matched objects and the positions of those that are missing (relative to Vargas Álvarez et al. 2013) over plotted on the g-band image.

Figure 5 is the highly magnified section of Figure 3 that contains the objects with known spectral type. The red and blue shaded regions are where we expect to find late-type (O9 - O6) and early-type (O6 - RJ) O stars respectively. We find that the majority of the objects are correctly separated into their respective early or late spectral-type zones defined by the $R_V = 3.8$ reddening tracks. This gives an early indication that an $R_V \sim 3.8$ reddening law is required for this sight-line and that the calibration of the data is in good agreement with the synthetic photometry.

Object #771 falls well above the 'RJ limit'. As a confirmed O8V star, its position in the $(u-g, g-r)$ diagram is clearly anomalous. Close inspection of the image suggests that the photometry of this star is affected by a bright neighbour.

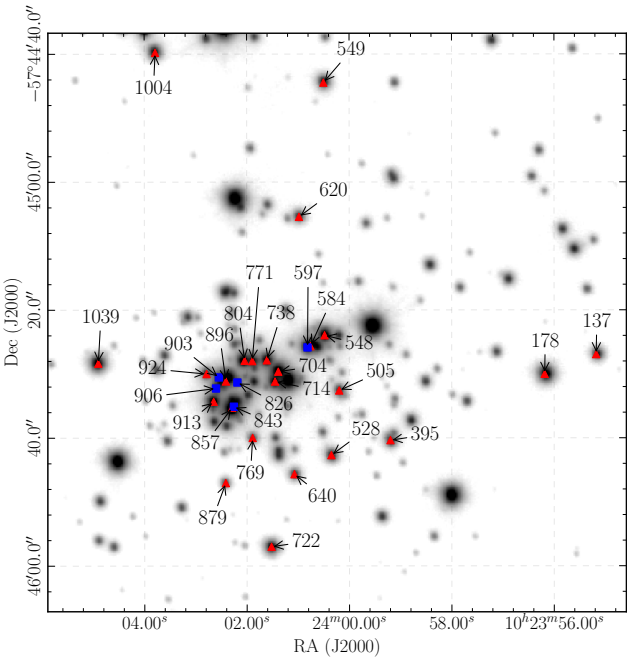

Figure 4. Inverse VPHAS+ g band image of the central region of Wd 2 showing the objects with known spectral type from Vargas Álvarez et al. (2013). The red triangles are the positions of the objects detected in VPHAS+ and the blue squares are the positions of those that are not detected due to crowding.

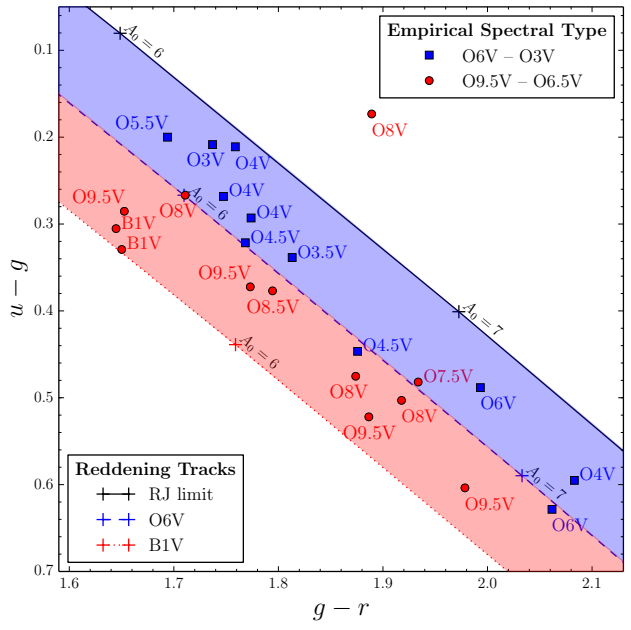

Figure 5. Testing the selection process of OB stars associated with Wd2. Objects with known spectral type tend to fall into the correct synthetic spectral type range with an $R_V = 3.8$ reddening law.

4.2 SED fitting

Ultimately 21 of the 24 known objects were suitable for SED fitting. These objects are tabulated in Table 2. Two of the objects left out are #896 and #771 for which there is no detection in one or more of the the optical bands due to blending. The third is object #1004 for which the near-infrared photometry is incomplete.

For each of the 21 objects for which we have computed SED fits, the posterior distribution was sampled with 100 *walkers* over 10000 *iterations* with a 1000 iteration burn in. The typical autocorrelation time for each walk (or number of steps per independent sample) was found to be well below 100, which indicates that the posteriors are thoroughly sampled. We can determine the probability distributions for each parameter by marginalising over all other parameters. We visualize this by constructing 1-D histograms of the values of each parameter visited in the random walk. We can also check for covariance or degeneracy between parameters by constructing marginalised 2-D histograms for each pair of parameters. Figure 6 shows an example of these diagrams for an O4V and a B1V star in the sample (#913 and #549).

The obvious difference between the two cases is apparent in the 1-D marginalisation of parameters. We see that the hotter the object the more skewed the probability distributions in $\log(T_{\rm eff})$ and μ become. This can be attributed to the fact that the hotter SEDs are approaching the RJ tail. This makes it more difficult to differentiate the temperature of the hottest stars and consequently the luminosity and distance. This makes the drop off in probability at the hot end more shallow. This intrinsic feature also means that the uncertainties on $\log(T_{\rm eff})$ and μ increase with temperature but has the positive effect of decreasing the uncertainties on A_0 and R_V. For the later type stars $\log(T_{\rm eff})$ is better defined but still uncertain.

The value adopted for each parameter is the median of the marginalised posterior distribution with upper and lower uncertainties defined by the 16$^{\rm th}$ and 84$^{\rm th}$ percentiles. We find that we are able to determine the values of A_0 and R_V with relatively high precision (better than ±0.09 mag and ±0.08 respectively in all cases). These uncertainties are similar to those found by Vargas Álvarez et al. (2013). We note that R_V and A_0 are well defined and show negligible covariance relative to each other and only modest covariance with respect to $\log(T_{\rm eff})$ and μ.

However, as expected, our determination of temperature and distance are not so informative. For object #913, $\log(T_{\rm eff}) = 4.59^{+0.08}_{-0.08}$ and $\mu = 12.91^{+0.97}_{-0.93}$. This corresponds to values of $T_{\rm eff} = 37^{+6.5}_{-4.8}$kK, or a spectral type range from O8.5V to O3V. The results for μ translate to $d = 3.8^{+2.1}_{-1.3}$kpc. This already significant distance uncertainty is nevertheless an underestimate given that neither the luminosity class or metallicity uncertainties have been formally incorporated. In addition we are treating all stars as if single which biases the inferred distance moduli to lower values by up to 0.75 mag. Because of the relative lack of constraint on $\log(T_{\rm eff})$ from the intrinsic colours of OB stars, the error in $\log(T_{\rm eff})$ is driven mainly by the error in μ. In comparison the direct effect of binarity on $\log(T_{\rm eff})$, through colour-changes, will be small. It is plainly apparent in Figure 6 that $\log(T_{\rm eff})$ and μ are strongly and positively covariant. The role of the distance modulus is essentially that of a normalisation parameter.

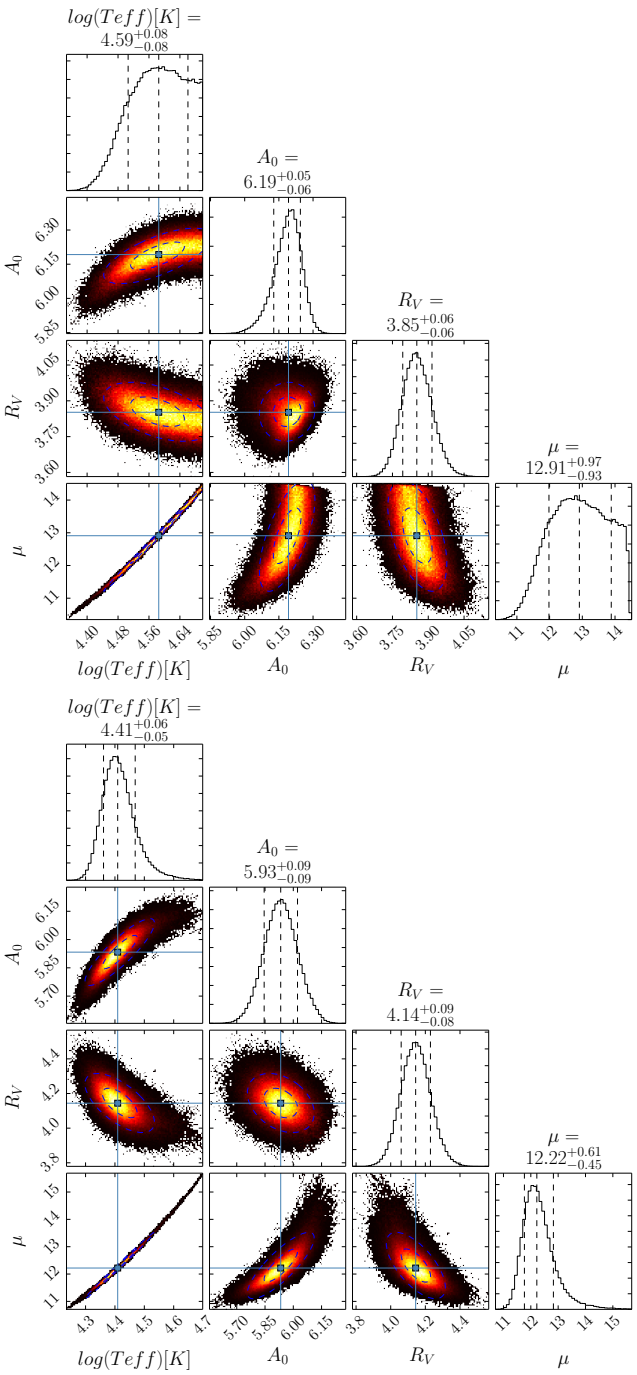

Figure 6. PDFs of the fitting parameters as a result of the MCMC simulation for stars #913 an O4V (top) and #549 and B1V (bottom) using the numbering system from Vargas Álvarez et al. (2013).

Figure 7 shows the results for the O4V star from Figure 6 translated into the original SED data space. The top panel shows the observed SED over-plotted by 30 randomly sampled model SEDs that are drawn from the posterior distributions shown in Figure 6. The lower panel shows the residuals between them. We can see that for each band, across all the

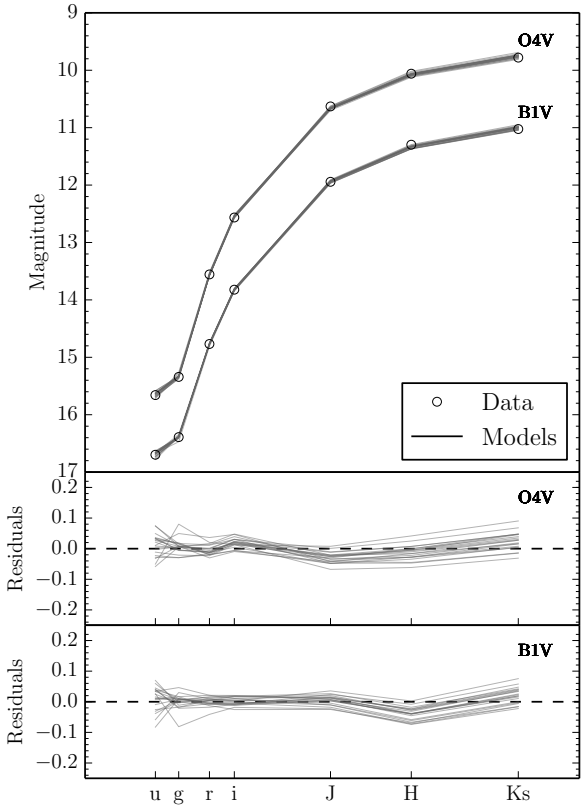

Figure 7. Visualisation of the posterior distributions of objects #913 and #549 (from Vargas Álvarez et al. 2013) in SED data space. The top panel shows 30 model SEDs for both objects (gray solid lines), generated from a random sampling of the posterior parameter distributions shown in Figure 6. Our photometric data is plotted on top (circles). The bottom panels show the residuals.

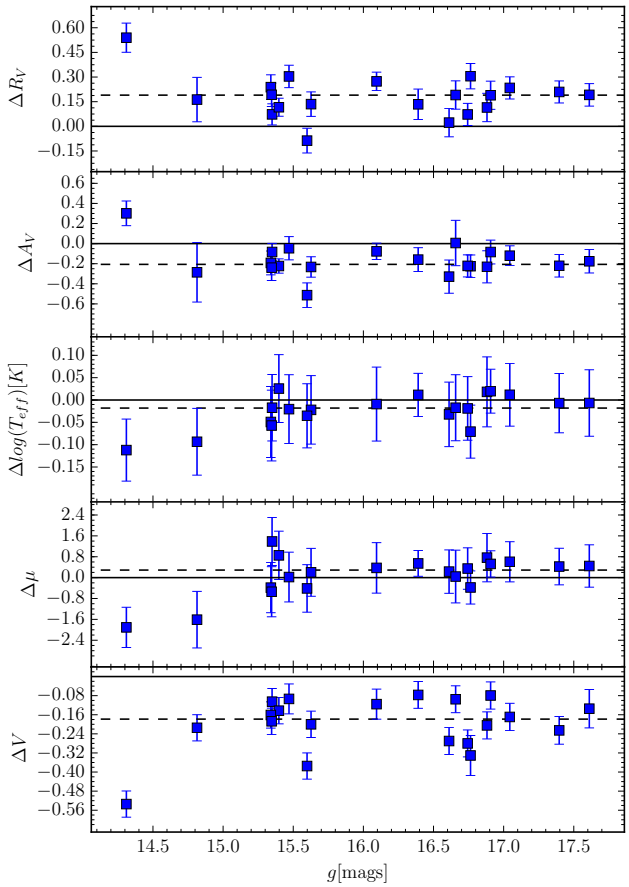

Figure 8. The difference between stellar parameters found in this study and those found by Vargas Álvarez et al. (2013). The solid line shows zero difference while the dashed line shows the median difference.

posterior distributions, the differences between the models and the data never exceed ~ 0.1 mag. The discrepancies between the model and data can be attributed to one or more of the following: inaccuracies in the intrinsic SEDs of OB stars in the Padova isochrones; inaccuracies in the shape of the reddening law; a calibration offset between the optical and NIR catalogues.

Table 2 compares the stellar parameters of the 21 known OB stars derived in this study with those from Vargas Álvarez et al. (2013). Here A_0 has been converted to A_V and the VPHAS+ g band magnitudes have been converted to V band using the Sloan to Johnson conversion from Lupton (2005)[2] for ease of comparison. We also note that our SED-derived $\log(T_{\rm eff})$ values are compared to spectroscopic values where available (Vargas Álvarez et al. 2013; Rauw et al. 2007). Otherwise effective temperatures are derived from spectral types according to the temperature scales of Martins et al. (2005) and Zorec & Briot (1991). We restrict our comparison to the results in Vargas Álvarez et al. (2013) based on the Fitzpatrick & Massa (2007) extinction curves.

Figure 8 plots the difference between the values derived in the two studies. It must be noted that star #584 has not been included in this analysis as extreme blending has substantially affected its photometry (see Figure 4 and Table 2).

A significant difference is found between the transformed V band magnitudes in VPHAS+ and HST of ~ 0.18 mag, such that VPHAS+ is brighter. Vargas Álvarez et al. (2013) compare their empirical B and V band measurements with those of Moffat et al. (1991) and Rauw et al. (2007) and find that those ground based measurements are also systematically brighter, by 0.18 and 0.15 mag, and by 0.22 and 0.12 respectively. Vargas Álvarez et al. (2013) suggest that the difference may be due to source blending following on from the effects of atmospheric seeing. If this were the case we would expect to find objects in the most crowded/blended region of the cluster to be consistently more discrepant. As we do not see this effect we suspect a real calibration difference. Hur et al. (2015) have also uncovered a similar problem but find good agreement between their optical photometry and that of Rauw et al. (2007). If the scale of Rauw et al. (2007) is the right one, our photometry may be too bright by ~ 0.05 mag.

[2] https://www.sdss3.org/dr8/algorithms/sdssUBVRITransform.php

Table 2. Table comparing the derived stellar parameters of objects with known spectral type from Vargas Álvarez et al. (2013) with the results in this study. The ID given corresponds to the numeration given by Vargas Álvarez et al. (2013) . Most of the effective temperatures in the HST column were derived spectroscopically by Vargas Álvarez et al. (2013) and uncertainties were given. The rest have no provided uncertainty as they were estimated from their spectral types using the temperature scales from Martins et al. (2005) and Zorec & Briot (1991).

ID	ST	A_V		R_V		$\log(T_{eff})$		μ		V	
		VPHAS+	HST	VPHAS+	HST	VPHAS+	HST	VPHAS+	HST	VPHAS+	HST
137	O4 V	$7.42^{+0.04}_{-0.05}$	7.41 ± 0.22	$4.03^{+0.05}_{-0.05}$	3.84 ± 0.07	$4.62^{+0.06}_{-0.07}$	4.633 ± 0.004	$13.23^{+0.75}_{-0.90}$	13.19 ± 0.45	$15.496 \pm +0.056$	15.591 ± 0.006
178	O4 V-III((f))*	$6.30^{+0.04}_{-0.05}$	6.38 ± 0.07	$4.00^{+0.06}_{-0.06}$	3.93 ± 0.03	$4.61^{+0.06}_{-0.07}$	4.629 ± 0.002	$13.17^{+0.78}_{-0.91}$	11.79 ± 0.16	$14.385 \pm +0.055$	14.490 ± 0.004
395	O7.5V*	$6.70^{+0.08}_{-0.09}$	6.92 ± 0.07	$4.08^{+0.07}_{-0.07}$	3.77 ± 0.03	$4.47^{+0.08}_{-0.06}$	4.544 ± 0.000	$12.41^{+0.90}_{-0.61}$	12.78 ± 0.18	$15.688 \pm +0.056$	16.019 ± 0.062
505	O8.5V	$6.13^{+0.06}_{-0.08}$	6.36 ± 0.14	$3.82^{+0.07}_{-0.06}$	3.71 ± 0.06	$4.55^{+0.09}_{-0.08}$	4.531 ± 0.006	$14.06^{+1.13}_{-0.88}$	13.29 ± 0.30	$15.889 \pm +0.056$	16.094 ± 0.005
528	O8 V	$6.64^{+0.07}_{-0.09}$	6.97 ± 0.14	$4.01^{+0.08}_{-0.07}$	3.99 ± 0.05	$4.51^{+0.10}_{-0.07}$	4.544 ± 0.005	$12.78^{+1.17}_{-0.77}$	12.55 ± 0.30	$15.571 \pm +0.056$	15.841 ± 0.005
548	O4 V	$6.29^{+0.05}_{-0.06}$	6.48 ± 0.10	$4.00^{+0.07}_{-0.06}$	3.76 ± 0.04	$4.58^{+0.08}_{-0.08}$	4.633 ± 0.002	$12.81^{+0.98}_{-0.93}$	13.19 ± 0.23	$14.361 \pm +0.055$	14.522 ± 0.002
549	B1 V*	$5.93^{+0.09}_{-0.09}$	6.09 ± 0.08	$4.14^{+0.09}_{-0.08}$	4.01 ± 0.04	$4.41^{+0.06}_{-0.05}$	4.398 ± 0.000	$12.22^{+0.61}_{-0.45}$	11.68 ± 0.19	$15.485 \pm +0.056$	15.562 ± 0.005
584	O8 V	$4.56^{+0.04}_{-0.05}$	6.19 ± 0.05	$2.88^{+0.04}_{-0.04}$	3.73 ± 0.02	$4.65^{+0.03}_{-0.05}$	4.544 ± 0.002	$15.19^{+0.46}_{-0.69}$	12.94 ± 0.12	$14.195 \pm +0.055$	15.442 ± 0.004
620	B1 V*	$5.69^{+0.09}_{-0.09}$	5.77 ± 0.08	$4.01^{+0.08}_{-0.08}$	3.82 ± 0.04	$4.42^{+0.06}_{-0.05}$	4.398 ± 0.000	$13.09^{+0.63}_{-0.47}$	12.56 ± 0.19	$16.007 \pm +0.057$	16.086 ± 0.006
640	O9.5V	$6.25^{+0.07}_{-0.09}$	6.37 ± 0.05	$3.96^{+0.07}_{-0.06}$	3.73 ± 0.02	$4.52^{+0.09}_{-0.07}$	4.505 ± 0.002	$13.72^{+1.13}_{-0.76}$	13.11 ± 0.13	$16.065 \pm +0.057$	16.234 ± 0.006
704	O4 V	$5.98^{+0.05}_{-0.06}$	6.27 ± 0.29	$3.92^{+0.07}_{-0.06}$	3.76 ± 0.12	$4.59^{+0.07}_{-0.07}$	4.681 ± 0.008	$12.65^{+0.91}_{-0.88}$	14.26 ± 0.63	$13.844 \pm +0.055$	14.059 ± 0.002
714	O3 V	$5.57^{+0.05}_{-0.05}$	6.08 ± 0.11	$3.64^{+0.06}_{-0.06}$	3.73 ± 0.05	$4.61^{+0.06}_{-0.07}$	4.643 ± 0.000	$14.11^{+0.79}_{-0.87}$	14.53 ± 0.26	$14.642 \pm +0.055$	15.017 ± 0.003
722	O6 V*	$7.15^{+0.06}_{-0.07}$	7.23 ± 0.04	$3.92^{+0.06}_{-0.06}$	3.65 ± 0.01	$4.57^{+0.08}_{-0.08}$	4.584 ± 0.001	$12.41^{+1.04}_{-0.96}$	12.04 ± 0.11	$14.944 \pm +0.055$	15.060 ± 0.030
738	O5.5V	$5.79^{+0.05}_{-0.06}$	6.02 ± 0.08	$3.87^{+0.07}_{-0.06}$	3.73 ± 0.04	$4.58^{+0.08}_{-0.08}$	4.602 ± 0.000	$13.59^{+0.98}_{-0.90}$	13.39 ± 0.19	$14.696 \pm +0.055$	14.896 ± 0.003
769	O9.5V	$6.41^{+0.08}_{-0.10}$	6.63 ± 0.06	$3.86^{+0.07}_{-0.06}$	3.65 ± 0.02	$4.48^{+0.09}_{-0.07}$	4.491 ± 0.002	$13.46^{+1.06}_{-0.69}$	13.04 ± 0.13	$16.351 \pm +0.057$	16.576 ± 0.008
804	O6 III*	$7.04^{+0.11}_{-0.11}$	6.91 ± 0.04	$4.09^{+0.10}_{-0.09}$	3.71 ± 0.01	$4.56^{+0.09}_{-0.08}$	4.582 ± 0.001	$11.74^{+1.08}_{-0.93}$	11.78 ± 0.10	$14.290 \pm +0.055$	14.433 ± 0.003
857	O4.5V	$6.43^{+0.09}_{-0.09}$	6.13 ± 0.08	$4.17^{+0.09}_{-0.08}$	3.63 ± 0.03	$4.51^{+0.09}_{-0.07}$	4.623 ± 0.002	$10.75^{+1.14}_{-0.75}$	12.65 ± 0.18	$13.335 \pm +0.055$	13.869 ± 0.003
879	O9.5V	$6.69^{+0.07}_{-0.09}$	6.98 ± 0.07	$3.81^{+0.07}_{-0.06}$	3.70 ± 0.03	$4.52^{+0.10}_{-0.08}$	4.519 ± 0.003	$13.77^{+1.19}_{-0.83}$	13.11 ± 0.16	$16.510 \pm +0.058$	16.645 ± 0.056
913	O3-4V*	$6.18^{+0.05}_{-0.07}$	6.42 ± 0.11	$3.85^{+0.06}_{-0.06}$	3.66 ± 0.04	$4.59^{+0.08}_{-0.08}$	4.642 ± 0.002	$12.91^{+0.97}_{-0.93}$	13.45 ± 0.24	$14.344 \pm +0.055$	14.531 ± 0.002
924	O8 V	$6.18^{+0.07}_{-0.09}$	6.40 ± 0.07	$3.67^{+0.06}_{-0.06}$	3.60 ± 0.03	$4.53^{+0.09}_{-0.07}$	4.544 ± 0.000	$13.51^{+1.14}_{-0.78}$	13.16 ± 0.16	$15.680 \pm +0.056$	15.960 ± 0.005
1039	O4-5V*	$6.37^{+0.05}_{-0.06}$	6.42 ± 0.10	$3.77^{+0.06}_{-0.06}$	3.47 ± 0.04	$4.60^{+0.07}_{-0.08}$	4.622 ± 0.002	$13.01^{+0.86}_{-0.93}$	12.98 ± 0.22	$14.429 \pm +0.055$	14.523 ± 0.030

The apparent systematic calibration difference between the two data sets is reflected in the derived values of A_V. In particular the median of the star-by-star differences in A_V shows that our extinctions are on average 0.18 mag less than those derived by Vargas Álvarez et al. (2013). The median A_V with the 16^{th} and 84^{th} percentiles in this study and in Vargas Álvarez et al. (2013) are; $A_V(\text{VPHAS+}) = 6.29^{-0.36}_{+0.42}$ and $A_V(\text{HST}) = 6.41^{-0.32}_{+0.56}$. With brighter optical magnitudes there is also an offset in R_V such that our values are higher: the median star-by-star difference in R_V is 0.19, while sample medians are respectively $R_V(\text{VPHAS+}) = 3.92^{-0.10}_{+0.11}$ and $R_V(\text{HST}) = 3.73^{-0.08}_{+0.11}$.

Despite the expectation of poor constraints on distance, the difference in the median values of μ happen to be very small: $\mu(\text{VPHAS+}) = 13.05 \pm 0.74$ and $\mu(\text{HST}) = 13.07 \pm 0.73$. This is likely to be due to the O stars in Wd 2 being on the main sequence, matching our assumption. Similarly there is only a modest offset on average in the measures of effective temperature.

The results of this comparison are encouraging. We have found good quantitative agreement, within the uncertainties, between our derived parameters and those of Vargas Álvarez et al. (2013) drawing on HST optical photometry. Where there are differences, we understand their origin. This gives us confidence that both our method and the underlying VPHAS+ data are producing reliable results.

5 RESULTS

Here we apply the SED fitting methods discussed above to the full selection of OB candidates from our pilot 2 sq.deg field.

5.1 'Goodness-of-fit'

The posterior distributions obtained tell us the most probable parameters given the data, however they do not tell us anything about 'goodness-of-fit'. As some objects in our selection may be contaminants or may just have bad photometry, it is important to determine how well the data fit the model in order to obtain a 'clean' selection of OB stars. We have opted to use the value of χ^2, given by the SED fits, at the median values in the marginalised posterior distribution. We are aware that the posterior medians may not exactly trace the maximum likelihood, but they provide a representative sample.

Figure 9 shows the χ^2 distribution of the fits to all 1108 objects in the wider selection above the distribution obtained for the known objects from Vargas Álvarez et al. (2013). Since we are fitting 7 data points with 4 parameters we expect a $k = 3$ χ^2 distribution peaking at 1 – the top panel of Figure 9 indicates this is what happens and, by implication, that the uncertainties on our data points are not significantly over- or under- estimated. In keeping with this, we have chosen to use the commonly adopted 5% significance level, at $\chi^2 = 7.82$ as the limit beyond which

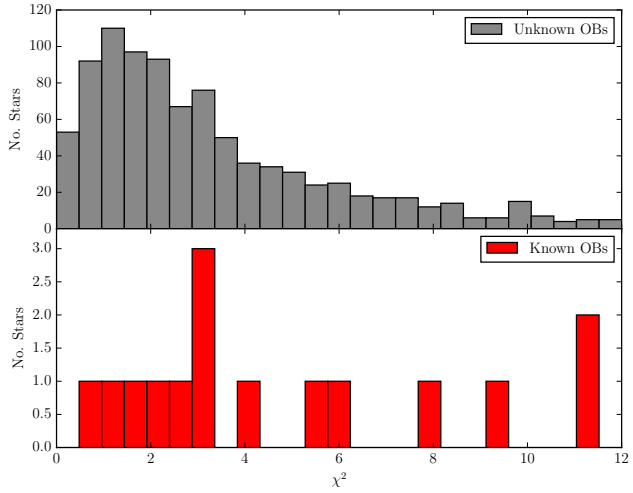

Figure 9. χ^2 distributions for the known objects (bottom) and the wider selection (top). The χ^2 distribution for the wider selection peaks at ~ 1 as a expected from a distribution with $k = 3$ degrees of freedom. Using a 5% significance level we judge objects with $\chi^2 > 7.82$ to be unsatisfactorily fit. The known objects with poor fits are subject to photometric blending in the clusters core.

we judge the fits to the applied model to be unsatisfactory. This cut makes reasonable sense when applied to the χ^2 distribution for the known objects (in common with Vargas Álvarez et al. 2013), in that the 10 confirmed OB stars beyond the chosen cut are mainly there because of the impact on the photometry of the blending in the crowded central parts of Wd 2 present in the VST data. For this reason we have still tabulated those objects not meeting our selection criteria but have not used them in any further analysis. We note that if both 2MASS Skrutskie et al. (2006) and Ascenso et al. (2007) photometry are available we keep which ever yields a better χ^2.

5.1.1 Further cross-matches with previously catalogued objects

All of the objects in the initial selection were cross-matched to $< 1''$ with the SIMBAD (Wenger et al. 2000) database to check for further examples of objects of known type.

Tsujimoto et al. (2007) conducted a 17×17 arcmin high resolution X-ray imaging survey centred on Wd2 and the surrounding star forming region RCW 49. They identified 17 new X-ray emitting OB candidates in this larger region, enclosing that studied by Vargas Álvarez et al. (2013). On using a 1" cross match radius we find 8 of these objects make it into our selection. Five of the missing objects are picked up by VPHAS+ but have $g < 13$ and hence were too bright to be selected. Conversely, the remaining 4 objects are detected by VPHAS+ but are too faint ($g > 20$) to be in our selection. It is likely that these objects are highly reddened.

Across all other literature sources, accessed via SIMBAD, fourteen further stars of confirmed type were found (see Table 3). The breakdown of their classifications is as follows: six stars with a Wolf-Rayet (WR) component, three OV, two OIII, one OVb, one B5Vne, one carbon star and one star listed as M1III. All six WR stars, the carbon star and one of the OV stars could not be fitted convincingly as reddened OB stars (i.e. $\chi^2 > 7.82$), while the others were ($\chi^2 < 7.82$). The OVb was confirmed as an O3V + O5.5V binary system by Vargas Álvarez et al. (2013) but was not used in their SED fitting analysis – hence it did not feature in Section 4.2. On close inspection of the literature, it became clear that the SIMBAD M1III attribution matching one of our selected objects is wrong, resulting from confusion over the sky position of the previously catalogued HAeBe candidate, THA 35-II-41. THA 35-II-41 is indeed one of our selected objects but it is not at the position attributed to it by Carmona et al. (2010) where these authors observed an M giant spectrum.

We also detect seven bright objects in the originally NIR selected open cluster DBS2003 45 (Dutra et al. 2003) centred at 10h19m10.5s $-58°02'22.6''$. The study by Zhu et al. (2009) identifies seven OB stars in this cluster estimated as ranging from spectral type B0 to O7 from low resolution NIR spectroscopy. However, six out of seven of the positions given in Table 2 of Zhu et al. (2009) do not match with the VPHAS+ positions nor with any detections in the 2MASS point source catalogue. We therefore suspect that there is an error in the positions that they give whilst our objects are in common. We find these are among the most highly extinguished objects in our selection with an average $A_V = 8.37$.

5.1.2 Summary of results

Figure 10 shows the stages in the selection process: first, those stars without a match to good quality NIR photometry have to be set aside (shown as grey crosses in the Figure); next, those with 'poor' χ^2 values (the cyan-coloured squares); finally the good fits are divided in two groups based on their effective temperature. Those with a a posterior median value of $\log(T_{\rm eff}) > 4.3$ - our target group of spectral type B2 and earlier - are shown as red triangles while those that are assigned cooler fits are shown as blue squares.

Counter-intuitively perhaps, it can be seen in Figure 10 that in the domain where $g - r < 0.5$, only 12 stars could be matched with good NIR photometry. This is because lowly reddened UV-excess objects detected in VPHAS+ are commonly too faint for detection in 2MASS due to their blue SEDs – for instance, some of these objects will be under-luminous hot compact objects. Unsurprisingly the cyan coloured squares representing objects with poor fits are frequently to be found above the Rayleigh-Jeans limit – only 2 objects with accepted fits just creep into this part of the diagram. It is reassuring that there is some offset between the $R_V = 3.1$ B3V reddening vector, serving as lower bound to the selection region, and the spread of hotter objects: it suggests that few, if any, stars hotter than $\log(T_{\rm eff}) = 4.3$ have been missed (given our other constraints, such as the magnitude limits). It is worth noting that the selection of objects that occupied the 0.1 mag wide band directly below the B3V reddening vector in $u - g$ provided just 1 star out of 374 with $\log(T_{\rm eff}) > 4.3$ and $\chi^2 < 7.82$.

The main groupings emerging from the fitting process of 1129 objects are as follows:

- 845 stars fit well as reddened OB stars ($\chi^2 < 7.82$)
  - 392 of these are in the hot group ($\log(T_{\rm eff}) > 4.3$)

Table 3. Objects crossed matched with SIMBAD in the selection which have known spectral type. Derived parameters of highly evolved objects will be inaccurate due to the main-sequence assumption as shown by their 'bad' χ^2 values. On further inspection of the literature the classification object #981 is much different from that in SIMBAD(see Section)

ID	RA	DEC	Identifier	Spectral Type	g	$\log(T_{eff})$	R_V	A_0	μ	χ^2
294	10 18 04.98	-58 16 26.27	WR 19	WC5+O9	14.02	$4.34^{+0.04}_{-0.04}$	$5.70^{+0.09}_{-0.09}$	$4.14^{+0.09}_{-0.09}$	$9.36^{+0.40}_{-0.40}$	38.77
349	10 18 53.39	-58 07 52.94	WR 19a	WN	15.45	$4.48^{+0.09}_{-0.09}$	$8.48^{+0.09}_{-0.09}$	$4.32^{+0.07}_{-0.07}$	$9.17^{+1.06}_{-1.06}$	9.78
452	10 20 17.50	-57 44 59.39	C* 1665	C*	16.54	$4.18^{+0.00}_{-0.00}$	$10.00^{+0.00}_{-0.00}$	$3.88^{+0.02}_{-0.02}$	$4.31^{+0.01}_{-0.01}$	2189.81
577	10 22 05.75	-57 53 46.03	2MASS J10220574-5753460	B5Vne	15.71	$4.38^{+0.05}_{-0.05}$	$5.55^{+0.09}_{-0.09}$	$3.80^{+0.07}_{-0.07}$	$11.64^{+0.53}_{-0.53}$	1.76
673	10 23 23.50	-58 00 20.80	SS 215	O2If*/WN5	13.48	$4.38^{+0.05}_{-0.05}$	$5.59^{+0.09}_{-0.09}$	$4.27^{+0.09}_{-0.09}$	$9.36^{+0.47}_{-0.47}$	15.39
720	10 23 58.01	-57 45 48.93	V* V712 Car	O3If*/WN6+O3If*/WN6	14.48	$4.44^{+0.07}_{-0.07}$	$7.40^{+0.09}_{-0.09}$	$4.27^{+0.07}_{-0.07}$	$8.93^{+0.69}_{-0.69}$	9.51
751	10 24 01.20	-57 45 31.03	Cl* Westerlund 2 MSP 188	O3V+O5.5V	14.34	$4.49^{+0.09}_{-0.09}$	$6.72^{+0.09}_{-0.09}$	$4.41^{+0.10}_{-0.10}$	$10.21^{+1.11}_{-1.11}$	5.48
777	10 24 02.44	-57 44 36.05	Cl Westerlund 2 5	O5/5.5V/III(f)	13.80	$4.50^{+0.09}_{-0.09}$	$5.88^{+0.08}_{-0.08}$	$4.24^{+0.09}_{-0.09}$	$10.71^{+1.00}_{-1.00}$	10.28
804	10 24 06.64	-57 47 15.88	Cl* Westerlund 2 NRM 3	O9.5V	17.61	$4.53^{+0.10}_{-0.10}$	$7.68^{+0.07}_{-0.07}$	$4.14^{+0.07}_{-0.07}$	$12.84^{+1.18}_{-1.18}$	1.94
827	10 24 16.25	-57 43 43.75	Cl* Westerlund 2 NRM 2	O8.5III	15.94	$4.60^{+0.07}_{-0.07}$	$7.33^{+0.05}_{-0.05}$	$4.00^{+0.05}_{-0.05}$	$12.45^{+0.88}_{-0.88}$	1.81
831	10 24 18.40	-57 48 29.77	WR 20b	WN6ha	14.61	$4.35^{+0.05}_{-0.05}$	$7.87^{+0.10}_{-0.10}$	$4.60^{+0.08}_{-0.08}$	$7.68^{+0.49}_{-0.49}$	21.16
835	10 24 21.29	-57 47 27.53	Cl* Westerlund 2 NRM 1	O6V	15.70	$4.63^{+0.05}_{-0.05}$	$7.00^{+0.04}_{-0.04}$	$4.12^{+0.06}_{-0.06}$	$13.01^{+0.63}_{-0.63}$	1.95
863	10 24 39.20	-57 45 21.20	2MASS J10243919-5745211	O5V	16.03	$4.59^{+0.08}_{-0.08}$	$6.98^{+0.05}_{-0.05}$	$3.98^{+0.06}_{-0.06}$	$12.74^{+0.98}_{-0.98}$	1.41
942	10 25 47.07	-58 21 27.66	THA 35-II-41	HAeBe	13.55	$4.54^{+0.09}_{-0.09}$	$4.11^{+0.06}_{-0.06}$	$4.76^{+0.13}_{-0.13}$	$13.16^{+1.09}_{-1.09}$	4.72
954	10 25 56.51	-57 48 43.54	WR 21a	WN+	13.62	$4.34^{+0.05}_{-0.05}$	$6.26^{+0.09}_{-0.09}$	$4.45^{+0.09}_{-0.09}$	$8.37^{+0.42}_{-0.42}$	41.17

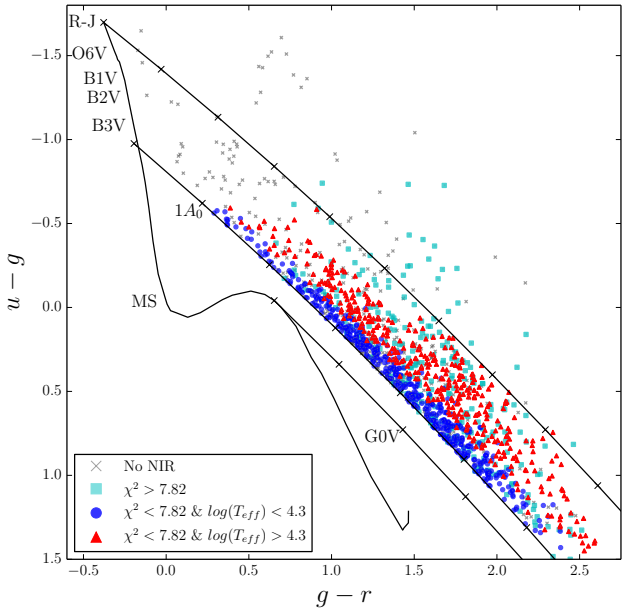

Figure 10. $(u-g, g-r)$ diagram showing the stages of selection. Red triangles are the final selection used for further discussion. All of the objects clearly above the RJ reddening vector are returned as bad fits.

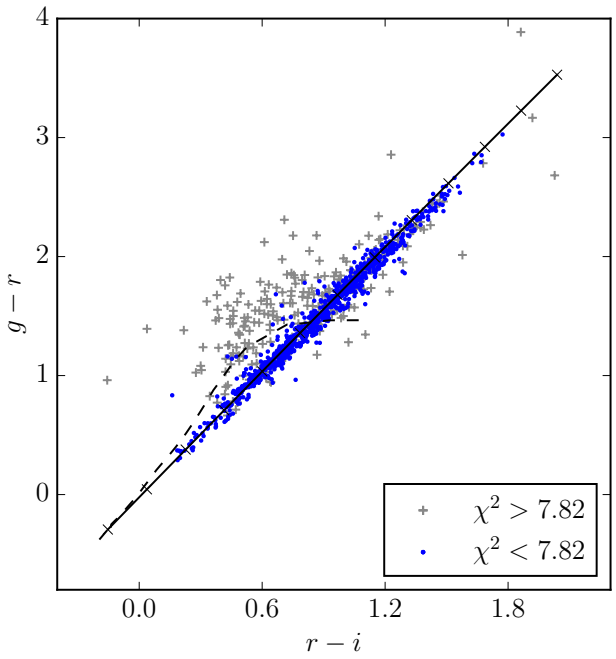

Figure 11. Positions of objects with $\chi^2 < 7.82$ (blue dots) and $\chi^2 < 7.82$ (grey crosses) in the $(r-i, g-r)$ plane. The solid black line is the reddening vector of an O9V with $R_V = 3.8$. The dashed line is the unreddened main sequence. We find that a large number of objects with 'poor' fits fall away from the OB star reddening vector. These objects show colours that are consistent with eclipsing W UMa contact binaries.

· 18 of these are known OB stars

· A further 18 have previously been identified as OB candidates.

– 453 of these are in the cool group ($\log(T_{\rm eff}) < 4.3$)

· 3 of these have previously been identified as OB candidates.

- 284 stars are judged poor fits ($\chi^2 > 7.82$)

– 167 are in the hot group and 117 are in the cool group.

· 11 of these are known OB stars (blending possible)

· 6 of these are known WR stars

· 1 of these is a carbon star with extremely red $g-r$

All of these objects along with their photometry and derived parameters are tabulated in Tables 4 and 5

Table 4: Sample table containing the positions and photometry of all 1129 objects. The first five columns are the objects IDs given in this study, VPHAS ID, Moffat et al. (1991), MSP ID, Vargas Álvarez et al. (2013), VA ID, Tsujimoto et al. (2007), TFT ID, and in SIMBAD, SIMBAD ID, where applicable. The full table can be found in the electronic version of this paper.

ID	MSP ID	VA ID	TFT ID	SIMBAD ID	ST	RA (J2000)	DEC (J2000)	u	err u	g	err g	r	err r	i	err i	Ha	err Ha	J	err J	H	err H	K	err K
1	–	–	–	–	–	10 13 09.25	-58 01 58.10	15.061	0.002	15.008	0.001	13.643	0.001	12.861	13.044	0.001	0.001	11.696	0.021	11.255	0.022	10.837	0.021
53	–	–	–	–	–	10 14 40.36	-57 24 26.24	16.937	0.006	15.487	0.001	12.959	0.001	11.468	12.345	0.001	0.001	8.693	0.024	7.870	0.036	7.414	0.027
95	–	–	–	–	–	10 15 24.77	-57 44 09.28	20.081	0.101	19.776	0.025	18.265	0.016	17.376	17.914	0.022	0.019	15.900	0.089	15.331	0.094	14.970	0.121
171	–	–	–	–	–	10 16 31.33	-57 48 18.68	19.199	0.034	18.923	0.010	17.323	0.006	16.565	17.392	0.017	0.007	15.246	0.054	14.763	0.079	14.509	0.096
173	–	–	–	–	–	10 16 31.97	-57 56 02.37	19.675	0.050	19.702	0.026	17.937	0.014	17.316	16.223	0.008	0.019	15.476	0.064	14.878	0.062	14.549	0.090
184	–	–	–	–	–	10 16 42.53	-57 32 47.65	17.559	0.009	16.168	0.002	13.576	0.001	12.078	13.053	0.001	0.001	9.327	0.026	8.474	0.049	7.953	0.027
428	–	–	–	–	–	10 19 47.82	-57 50 38.64	17.677	0.014	17.057	0.004	15.127	0.002	13.894	14.697	0.003	0.001	11.830	0.026	11.179	0.027	10.872	0.027
511	–	–	–	–	–	10 21 20.56	-57 43 09.40	15.521	0.003	15.231	0.001	13.666	0.001	12.692	13.284	0.001	0.001	11.014	0.023	10.524	0.023	10.292	0.021
602	–	–	–	–	–	10 22 19.90	-57 46 11.21	17.855	0.011	16.506	0.002	14.037	0.001	12.592	13.513	0.001	0.001	9.870	0.024	9.100	0.024	8.600	0.021
627	–	–	–	–	–	10 22 35.02	-58 33 37.82	16.554	0.005	16.692	0.002	15.716	0.002	15.153	15.471	0.004	0.002	14.220	0.056	13.883	0.066	13.810	0.064
710	182	178	112	Cl* Westerlund 2 MSP 182	O4III	10 23 56.18	-57 45 30.00	15.587	0.004	15.349	0.002	13.624	0.001	12.613	13.211	0.001	0.001	10.520	0.015	10.050	0.008	9.750	0.020
746	157	584	–	2MASS J10240073-5745253	O6.5V	10 24 00.76	-57 45 25.65	15.376	0.004	15.137	0.002	13.450	0.001	12.437	13.044	0.001	0.001	11.660	0.038	11.150	0.027	10.790	0.031
758	263	722	202	Cl* Westerlund 2 MSP 263	O6V	10 24 01.52	-57 45 57.00	16.696	0.008	16.094	0.003	14.055	0.001	12.859	13.633	0.002	0.001	10.520	0.025	9.910	0.035	9.530	0.036
766	167	804	217	Cl* Westerlund 2 MSP 167	O8V	10 24 02.04	-57 45 27.94	15.858	0.005	15.398	0.002	13.430	0.001	12.306	13.007	0.001	0.001	9.960	0.122	9.357	0.158	8.982	0.095
771	203/444	857	224	Cl* Westerlund 2 NRM 4	O9.5I	10 24 02.29	-57 45 35.26	14.604	0.003	14.310	0.001	12.566	0.001	11.560	12.170	0.001	0.001	9.450	0.063	8.950	0.090	8.520	0.050
797	171	1039	298	Cl* Westerlund 2 MSP 171	O5V	10 24 04.90	-57 45 28.35	15.886	0.005	15.470	0.002	13.616	0.001	12.552	13.206	0.001	0.001	10.480	0.018	10.000	0.039	9.740	0.033
804	383	–	314	Cl* Westerlund 2 NRM 3	O9.5V	10 24 06.64	-57 47 15.88	18.263	0.023	17.608	0.006	15.502	0.003	14.248	14.952	0.003	0.002	11.736	0.028	11.008	0.025	10.536	0.023
827	–	–	388	Cl* Westerlund 2 NRM 2	O8.5III	10 24 16.25	-57 43 43.75	16.495	0.007	15.936	0.003	13.883	0.001	12.664	13.432	0.001	0.001	10.316	0.023	9.624	0.023	9.236	0.021
835	–	–	405	Cl* Westerlund 2 NRM 1	O6V	10 24 21.29	-57 47 27.53	16.048	0.006	15.703	0.002	13.796	0.001	12.636	13.367	0.001	0.001	10.435	0.024	9.745	0.022	9.386	0.019
863	–	–	447	2MASS J10243919-5745211	O5V	10 24 39.20	-57 45 21.20	16.519	0.007	16.033	0.003	14.084	0.001	12.919	13.644	0.002	0.001	10.709	0.026	10.060	0.027	9.679	0.023

Table 5: Sample table containing the derived parameters of all 1129 objects. The $16^{\rm th}$, $50^{\rm th}$ and $84^{\rm th}$ percentiles are given for each parameter as well as the χ^2 value at the $50^{\rm th}$ percentile. The notes column indicates if the object shows emission (EM), is a sub-luminous candidate (SUB), is a blue supergiant candidate (BSG) or is a new O star candidate near Wd 2 (WD2) with similar reddening. The full table can be found in the electronic version of this paper.

ID	$\log(T_{\rm eff})$ $16^{\rm th}$	$\log(T_{\rm eff})$ $50^{\rm th}$	$\log(T_{\rm eff})$ $84^{\rm th}$	A0 $16^{\rm th}$	A0 $50^{\rm th}$	A0 $84^{\rm th}$	RV $16^{\rm th}$	RV $50^{\rm th}$	RV $84^{\rm th}$	DM $16^{\rm th}$	DM $50^{\rm th}$	DM $84^{\rm th}$	χ^2	Notes
1	4.36	4.41	4.36	4.46	4.55	4.46	3.66	3.74	3.66	11.90	12.33	11.90	37.41	EM
53	4.28	4.32	4.28	8.15	8.24	8.15	3.73	3.77	3.73	7.24	7.56	7.24	2.70	EM/BSG
95	4.27	4.31	4.27	4.91	5.05	4.91	3.72	3.85	3.72	15.15	15.52	15.15	2.46	SUB
171	4.34	4.37	4.34	4.55	4.64	4.55	3.33	3.41	3.33	15.31	15.61	15.31	6.40	SUB
173	4.37	4.39	4.37	5.46	5.55	5.46	4.14	4.24	4.14	15.42	15.69	15.42	41.01	EM
184	4.33	4.37	4.33	8.34	8.44	8.34	3.72	3.77	3.72	8.20	8.62	8.20	1.09	BSG
428	4.47	4.56	4.47	6.69	6.77	6.69	3.70	3.76	3.70	12.65	13.64	12.65	7.37	WD2
511	4.42	4.48	4.42	5.44	5.53	5.44	3.69	3.75	3.69	11.64	12.32	11.64	5.07	WD2
602	4.28	4.33	4.28	7.99	8.09	7.99	3.75	3.80	3.75	8.53	8.87	8.53	2.65	BSG
627	4.30	4.34	4.30	3.30	3.39	3.30	3.57	3.69	3.57	14.33	14.66	14.33	1.01	SUB
710	4.54	4.61	4.54	6.26	6.31	6.26	3.95	4.00	3.95	12.27	13.17	12.27	24.17	–
746	4.60	4.65	4.60	4.52	4.56	4.52	2.84	2.88	2.84	14.50	15.19	14.50	70.32	–
758	4.49	4.57	4.49	7.11	7.18	7.11	3.87	3.92	3.87	11.45	12.41	11.45	8.14	–
766	4.48	4.56	4.48	6.96	7.07	6.96	4.00	4.09	4.00	10.81	11.74	10.81	1.19	–
771	4.44	4.51	4.44	6.35	6.44	6.35	4.09	4.17	4.09	10.00	10.75	10.00	2.14	–
797	4.52	4.60	4.52	6.33	6.39	6.33	3.72	3.77	3.72	12.08	13.01	12.08	18.31	–
804	4.45	4.53	4.45	7.59	7.68	7.59	4.08	4.14	4.08	11.99	12.84	11.99	1.94	–
827	4.52	4.60	4.52	7.27	7.33	7.27	3.95	4.00	3.95	11.50	12.45	11.50	1.81	–
835	4.56	4.63	4.56	6.95	7.00	6.95	4.06	4.12	4.06	12.17	13.01	12.17	1.95	–
863	4.51	4.59	4.51	6.91	6.98	6.91	3.93	3.98	3.93	11.79	12.74	11.79	1.41	–

5.1.3 *Contaminants*

The ($\chi^2 > 7.82$) fits have a range of causes. The most frequent are likely to be contact binaries or the products of poor photometry.

Contact binaries may find their way into the selection because they are both quite common and rapidly variable. Figure 11 shows how around half of the $\chi^2 < 7.82$ objects clearly separate in the $(r-i, g-r)$ colour-colour diagram away from the OB stars towards redder $g-r$ at fixed $r-i$. This is plausibly the signature of contact binary (W UMa) interlopers. W UMa systems are doubly eclipsing binaries in which the brightness in any one band scarcely remains constant over time. These objects have typical orbital periods of 8 hours with two pronounced minima per cycle (Rucinski 1992). The u/g/r VST exposures are taken sequentially with about 15 minutes elapsing between u and g, and g and r. If the g band exposure of a W UMa system is taken at or near minimum light, its measured $u-g$ colour is bluer than true, while $g-r$ is redder, potentially pushing the star up into our OB selection. However these objects fail to pass as OB stars when the whole OnIR SED fit is performed, hence their poor χ^2 values. It has been estimated that there is around 1 W UMa system for every ~ 130 main sequence stars (Rucinski 1992). So finding perhaps as many as ~ 100 in our OB selection, given ~ 100000 stars across the 2 square degrees with $u/g/r$ photometry, is reasonable.

The second common origin for the poor fits is likely due to photometry affected by blending or incorrect cross-matching between bands. In the crowded core of Wd 2 this is an obvious difficulty (see Figures 4 and 10).

The literature search already reported in section 5.1.2 revealed that high χ^2 may be linked to extreme objects like WR stars (6 examples) and carbon stars (1 only). Another rare contaminant may be white dwarf/M dwarf binaries that can present blue $u-g$, alongside red $r-i$. The blue white-dwarf light begins to be overwhelmed by the red dwarf's light with increasing wavelength, shifting the combined colours below and to the right of the OB reddening track in the $(g-r, r-i)$ diagram (fig 11). Such objects are known to co-locate with reddened OB stars in the $(u-g, g-r)$ diagram or they may fall beyond the RJ reddening vector (Smolčić et al. 2004).

5.2 Parameters of the candidate OB stars ($\chi^2 < 7.82$ and $\log(T_{\rm eff}) > 4.3$)

Figure 12 shows the distribution of stellar parameters across the entire selection for the objects fitting to a reddened OB-star SED with $\chi^2 < 7.82$. Coloured in red are the results for all objects within an 8 arcmin box centred on Wd 2 (drawn in Figure 17). It can be seen that those objects in or near the cluster are reported to have similar extinction in the range $5.5 \leqslant A_0 \leqslant 7$ (top right panel in Figure 12). Otherwise, the reddenings range more broadly across the full 2 square degrees from $A_0 \simeq 3$ up to $A_0 \simeq 8$. Other features of this particular sight-line are that larger than standard R_V is favoured – a roughly normal distribution in R_V about a mean value of $R_V = 3.84 \pm 0.25$ is obtained – and that most of the selected stars are attributed distances of between ~ 2 kpc ($\mu \simeq 11$) and ~ 6 kpc ($\mu \simeq 14$). The objects in/near Wd2 tend toward the higher end of the distance modulus range and show a fairly wide spread in extinction law with $3.5 \leqslant R_V \leqslant 4.5$.

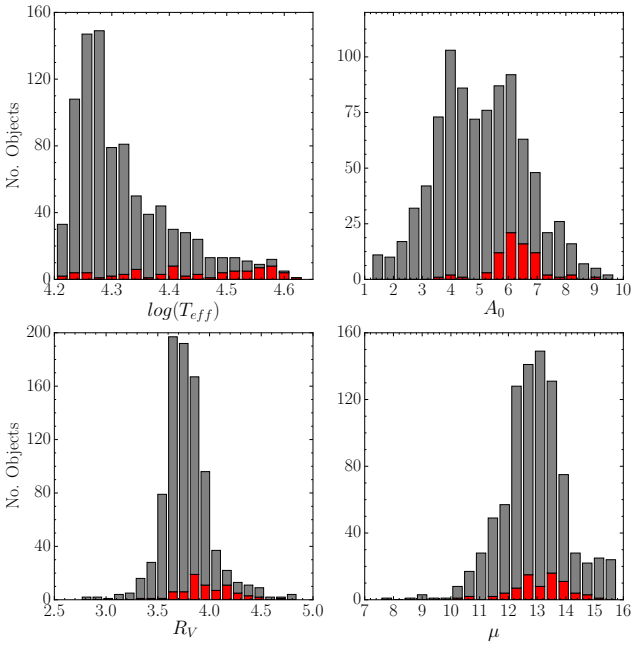

Figure 12. Distribution of the best fit parameters for the selection of objects with $\chi^2 < 7.82$. The red bars are objects within and 8 arcmin box of Wd 2 while the grey bars are the wider selection. We find that the objects spatially associated with Wd 2 show a tight distribution in A_0 and provide an over density of objects in the $5.5 \leqslant A_0 \leqslant 7$ range and also show a wider spread in R_V.

Echoing the initial mass function (IMF), the distribution in $\log(T_{\rm eff})$ is heavily skewed towards the lower values. Predictably, the hottest candidates are mainly stars in and around Wd 2: this young massive cluster does indeed stand out in this part of the Galactic Plane. The turn over in the $\log(T_{\rm eff})$ distribution at just below $\log(T_{\rm eff}) = 4.3$ further supports the conclusion that our initial selection of VPHAS+ sources in the $(u-g, g-r)$ diagram is essentially complete in the desired O to B2 effective temperature range (given our magnitude limits). The coolest object in the candidate list is ∼16000 K.

Figure 13 shows the upper and lower uncertainties on each parameter as a function of g-band magnitude for all $\chi^2 < 7.82$ objects. The uncertainty on $\log(T_{\rm eff})$ and A_0 increases for fainter objects, tracking the increase with rising magnitude of the photometric errors. Conversely the uncertainty on R_V shows a slight increase with decreasing magnitude at the bright end. R_V is more difficult to determine for bright objects as they tend to be less obscured. Nevertheless it is evident that both R_V and A_0 are consistently well determined across the entire magnitude range. Our OnIR SED fits deliver A_0 to within $\lesssim 0.09$ mag up to 18^{th} magnitude, rising up to $\lesssim 0.25$ mag at 20^{th} magnitude. We find the median uncertainty on R_V to be 0.081.

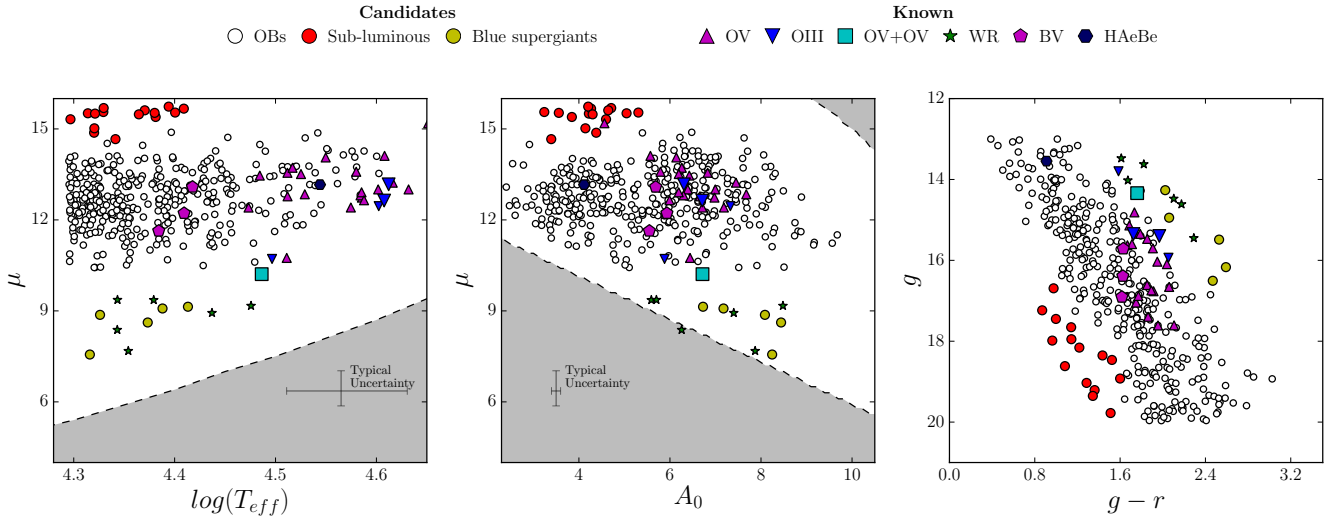

Figure 14. 2-D distribution of the best fit parameters for the final selection of OB candidates ($\chi^2 < 7.82$ and $\log(T_{\rm eff}) > 4.3$) and objects in the selection with known spectral type (the carbon star lays outside the range of 2 of these diagrams and was therefore not included). Objects shown in red and yellow are thought to be candidate sub-luminous OB stars and candidate blue supergiants respectively. The areas shaded in grey are where we cannot detect OB stars given the survey limits

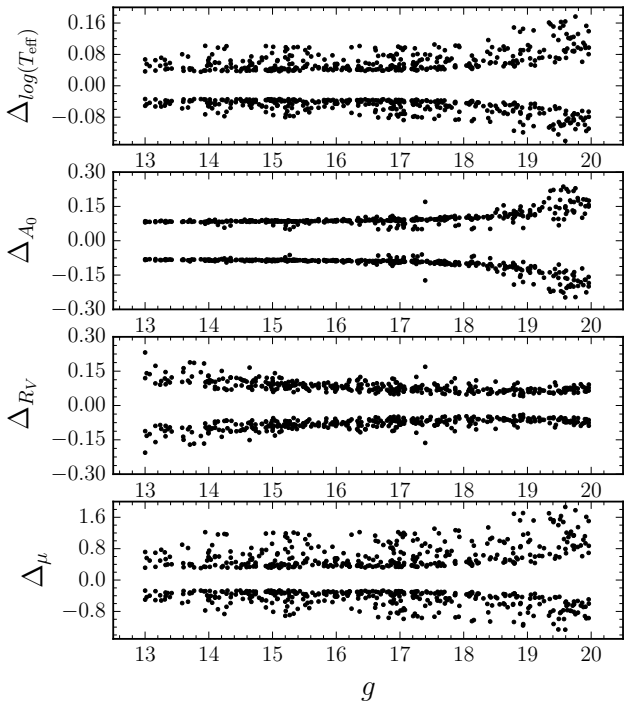

Figure 13. Uncertainty on each parameter as a function of g band magnitude. Uncertainties are derived from the $16^{\rm th}$ and $84^{\rm th}$ percentiles of the posterior distributions.

5.3 Inferences from the best-fit parameters and other aspects of the photometry

A richer understanding of the candidate objects can be obtained from a combination of more scrutiny of the fit parameters obtained and from a fuller utilisation of the VPHAS+ photometry at our disposal. So far the focus has been on the information to be extracted from the individual OnIR SEDs – treating all candidates as if they are well described as reddened, single, main-sequence OB stars. We can learn more through consideration of the ensemble of objects, and if use is made of the narrowband Hα band to separate out emission line stars.

First we acknowledge and relax the main sequence assumption applied so far. The first two panels of Figure 14 show scatter plots of the best-fit median distance modulus, μ, vs. $\log(T_{\rm eff})$ and vs. A_0 for the candidate OB stars. Different symbols are over-plotted to pick out the already known objects listed in SIMBAD as well as the O stars of Vargas Álvarez et al. (2013). The areas shaded in grey are where we cannot detect OB stars given the survey limits. The objects plotted as red circles have relatively low extinction but, if we take the returned distance moduli at face value, they would have to be construed as very distant (> 10 kpc) when compared to the known OB stars. It is more plausible that these are intrinsically sub-luminous objects rather than distant OB stars located in remarkably clear reddening holes. Their scattered spatial distribution across the whole field shown in Figure 17 supports this argument.

The converse argument can be applied to those objects plotted as yellow circles: they are found to have more than 6 magnitudes of extinction but are seemingly very close (less than ∼700pc away, $\mu < 9$). We suspect that these objects are intrinsically much higher-luminosity, evolved B stars. The proximity of these stars in the figures to the (poorly-fit) known WR stars, including the highly-luminous WR20a, lends credibility to this interpretation.

Referring back to the photometry in the form of a $(g, g-r)$ colour magnitude diagram (CMD), these interpretations are seen to make sense – the sub-luminous and over-luminous objects form tracks separated from the main-sequence – see the third panel of Figure 14. Table 6 lists these extreme objects. There will be further discussion of them in Section 6. The main concentration of objects ap-

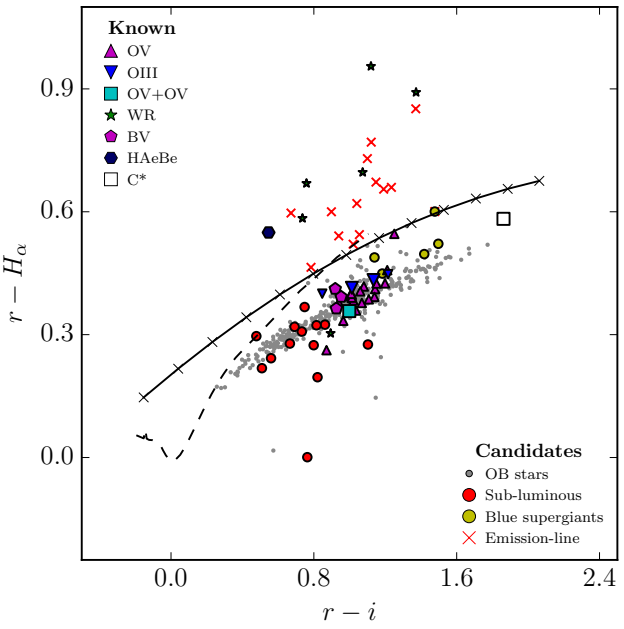

Figure 15. 13 of the $\chi^2 < 7.82$ and $\log(T_{\rm eff}) > 4.3$ objects show Hα excess. As emission is usually associated with circumstellar dust; the derived extinction may be incorrect. The solid line is the reddening vector of an O9V raised by 0.1 in $r - H\alpha$.

pears in the $11.5 < \mu < 14$ mag range which equates to distances ranging from $2 - 6$kpc. This encloses the derived distance range of the Carina arm traced in CO by Grabelsky et al. (1988), near its tangent.

We can also use the VPHAS+ Hα measurements to uncover any emission line stars in our selection. The presence of emission lines implies the presence of ionized circumstellar gas which, among massive OB stars, most commonly indicates classical Be stars with circumstellar disks. Although the OnIR SEDs of classical Be stars are not greatly different from normal B stars of similar effective temperature, the derived interstellar extinctions from SED fits that do not take into account the circumstellar continuum emission will nevertheless be overestimated. We have used the $(r - i, r -$ H$\alpha)$ diagram to select all objects that lie more than 0.1 mag in $r -$Hα above the O9V reddening vector (this equates to $\sim 10\AA$ in emission line equivalent width). Figure 15 shows this selection. Using the relation between EW(Hα) and added colour excess $E(B - V)$ due to the presence of a circumstellar disk in classical Be stars from Dachs et al. (1988), we can estimate that the derived reddenings (A_0) for our Hα-excess stars will have been inflated by between ∼0.1 and ∼0.3 magnitudes. There are 13 of these objects in the $\chi^2 < 7.82$ and $\log(T_{\rm eff}) > 4.3$ group and a further 63 with $\chi^2 > 7.82$ and/or $\log(T_{\rm eff}) < 4.3$. Objects with Hα excess are marked in Table 5.

5.4 Reddening

After removing the obvious sub/over-luminous objects and the emission line stars from the selection we are left with a cleaner selection of 365 ∼ non-emission OB candidates and 17 known OB stars available for further examination of their reddening properties.

Given our tight grasp on A_0 and R_V, it is of interest to consider their interdependence. R_V is plotted as a function of A_0 in Figure 16. The left panel of this Figure includes those objects within an 8 arcmin box around Wd 2 and the right hand panel excludes them. The areas shaded in grey are where we cannot detect OB stars given the survey limits. In both cases we can see a moderate positive correlation in R_V as a function of A_0 (correlation coefficient $r = 0.47$ and $r = 0.45$ respectively). On comparing the two panels, it is evident that the members of Wd 2 drive up the R_V trend more sharply when they are included. The shaded background shows that the trends seen are independent of the boundaries set by the survey selection limits. Given that it was demonstrated in Section 4.2 that the fitting method generates negligible covariance between A_0 and R_V, we can say with confidence that the correlation apparent now is related to the physical nature of the volume of space under study.

It is commonly accepted that increasing R_V is linked to increasing typical dust grain size, and that values of 3.5 and more are associated with denser molecular cloud environments (see e.g. Draine 2003). The 2 square degrees under examination here sample sight-lines lying just inside the Carina Arm tangent direction. Our pencil beam is evidently one that would initially pass through the atomic diffuse interstellar medium and then enter the dense clouds of the Carina Arm, wherein Wd 2 is located. In this situation it makes sense that as the dust column grows it becomes ever more dominated by the dense/molecular ISM component – i.e. R_V tends to rise. However the rise is not dramatic, and the data points show significant dispersion, which may imply that the variation in the dust properties within the sampled volume is not especially coherent. The effect of the bright limit of the survey is to remove sensitivity to A_0 much below 2–3, or to distances less than ∼3 kpc (see below). Current maps of Galactic spiral arm structure place this distance already within the Carina Arm (Russeil 2003; Vallée 2014).

The clear message of Figure 16 is that the typical, if necessarily idealised, reddening law for this sight-line is $R_V \sim 3.8$, which rises much less sharply with decreasing wavelength than the Galactic average of $R_V = 3.1$ (see Figure 13 in Fitzpatrick & Massa 2007).

6 DISCUSSION

6.1 The number and spatial distribution of the OB candidates

Figure 17 shows the location of each new candidate in the 2 square degrees for which the SED fit returned $\chi^2 < 7.82$ and $\log(T_{\rm eff}) > 4.3$, over-plotted on the VPHAS+ Hα mosaic. Each star is colour-coded according to its derived extinction, A_0. The 402 objects are scattered across the field, with lower reddenings ($A_0 < 5$) dominating in the southern half. Apart from in Westerlund 2 itself, the distribution is sparser and more highly-reddened in the north. Towards the NW and the tangent direction, roughly at RA 10h11m, Dec -56 14 (J2000) (Dame 2007), the most reddened objects ($A_0 > 8$) are found.

Table 6. Table containing the derived stellar parameters of the sub-luminous and blue supergiant candidates in the $\chi^2 < 7.82$ and $\log(T_{\rm eff}) > 4.3$ group.

ID	RA	DEC	g	$log(T_{eff})$	A_0	R_V	μ	χ^2
Sub-Luminous								
95	10 15 24.77	-57 44 09.28	19.78	$4.31^{+0.03}_{-0.03}$	$5.05^{+0.13}_{-0.13}$	$3.85^{+0.13}_{-0.13}$	$15.52^{+0.27}_{-0.27}$	2.46
102	10 15 36.78	-57 46 58.03	17.65	$4.33^{+0.03}_{-0.03}$	$3.24^{+0.09}_{-0.09}$	$3.16^{+0.10}_{-0.10}$	$15.56^{+0.23}_{-0.23}$	0.96
171	10 16 31.33	-57 48 18.68	18.92	$4.37^{+0.02}_{-0.02}$	$4.64^{+0.09}_{-0.09}$	$3.41^{+0.09}_{-0.09}$	$15.61^{+0.20}_{-0.20}$	6.40
211	10 17 01.28	-58 05 29.31	19.35	$4.33^{+0.02}_{-0.02}$	$4.71^{+0.13}_{-0.13}$	$4.03^{+0.14}_{-0.14}$	$15.69^{+0.15}_{-0.15}$	6.14
306	10 18 11.80	-58 20 12.24	19.21	$4.30^{+0.04}_{-0.04}$	$4.60^{+0.13}_{-0.13}$	$3.84^{+0.14}_{-0.14}$	$15.32^{+0.33}_{-0.33}$	1.72
483	10 20 48.03	-57 45 45.52	18.35	$4.32^{+0.04}_{-0.04}$	$4.38^{+0.12}_{-0.12}$	$3.47^{+0.12}_{-0.12}$	$14.87^{+0.42}_{-0.42}$	0.26
487	10 20 53.73	-57 58 41.78	17.95	$4.41^{+0.02}_{-0.02}$	$4.27^{+0.08}_{-0.08}$	$4.08^{+0.11}_{-0.11}$	$15.67^{+0.17}_{-0.17}$	4.84
499	10 21 07.91	-57 33 52.74	18.16	$4.39^{+0.01}_{-0.01}$	$4.20^{+0.08}_{-0.08}$	$3.88^{+0.10}_{-0.10}$	$15.73^{+0.12}_{-0.12}$	6.52
501	10 21 10.28	-58 10 46.02	18.62	$4.32^{+0.03}_{-0.03}$	$4.22^{+0.10}_{-0.10}$	$4.39^{+0.16}_{-0.16}$	$15.50^{+0.26}_{-0.26}$	1.54
627	10 22 35.02	-58 33 37.82	16.69	$4.34^{+0.04}_{-0.04}$	$3.39^{+0.09}_{-0.09}$	$3.69^{+0.13}_{-0.13}$	$14.66^{+0.40}_{-0.40}$	1.01
676	10 23 27.84	-57 54 56.79	19.03	$4.40^{+0.03}_{-0.03}$	$5.31^{+0.08}_{-0.08}$	$4.53^{+0.11}_{-0.11}$	$15.54^{+0.25}_{-0.25}$	6.25
886	10 24 58.98	-57 59 56.24	17.45	$4.38^{+0.03}_{-0.03}$	$3.85^{+0.14}_{-0.14}$	$4.19^{+0.20}_{-0.20}$	$15.39^{+0.33}_{-0.33}$	1.28
915	10 25 25.08	-57 59 04.50	17.98	$4.32^{+0.04}_{-0.04}$	$4.14^{+0.12}_{-0.12}$	$4.85^{+0.11}_{-0.11}$	$15.02^{+0.33}_{-0.33}$	2.60
1080	10 28 14.60	-57 41 36.33	17.24	$4.38^{+0.03}_{-0.03}$	$3.56^{+0.13}_{-0.13}$	$4.39^{+0.22}_{-0.22}$	$15.53^{+0.26}_{-0.26}$	2.65
1115	10 28 56.00	-58 09 02.55	18.46	$4.36^{+0.03}_{-0.03}$	$4.30^{+0.09}_{-0.09}$	$3.30^{+0.09}_{-0.09}$	$15.48^{+0.28}_{-0.28}$	5.87
Blue supergiants								
53	10 14 40.36	-57 24 26.24	15.49	$4.32^{+0.05}_{-0.05}$	$8.24^{+0.10}_{-0.10}$	$3.77^{+0.05}_{-0.05}$	$7.56^{+0.40}_{-0.40}$	2.70
184	10 16 42.53	-57 32 47.65	16.17	$4.37^{+0.06}_{-0.06}$	$8.44^{+0.10}_{-0.10}$	$3.77^{+0.05}_{-0.05}$	$8.62^{+0.54}_{-0.54}$	1.09
197	10 16 53.91	-57 55 02.11	14.26	$4.41^{+0.06}_{-0.06}$	$6.73^{+0.09}_{-0.09}$	$3.82^{+0.06}_{-0.06}$	$9.14^{+0.64}_{-0.64}$	0.19
467	10 20 31.60	-58 03 08.72	14.95	$4.39^{+0.06}_{-0.06}$	$7.18^{+0.09}_{-0.09}$	$4.03^{+0.07}_{-0.07}$	$9.08^{+0.55}_{-0.55}$	1.07
602	10 22 19.90	-57 46 11.21	16.51	$4.33^{+0.05}_{-0.05}$	$8.09^{+0.10}_{-0.10}$	$3.80^{+0.05}_{-0.05}$	$8.87^{+0.42}_{-0.42}$	2.65

378 of the objects shown have not been identified previously as candidate OB stars. Previous works by Reed (2003), and by Kaltcheva & Golev (2012) have noted 26 stars earlier than B3 within this region – all of which are brighter than $V = 11$, and therefore not in our sample. Also for reasons of brightness, our sample does not include any stars obviously associated with IC 2581. Turner (1978) studied the cluster – home to a number of early B stars – establishing a distance of 2.87 kpc, and a typical reddening corresponding to $A_0 \sim 1.5$. For the present selection, this cluster is too close and too lowly-reddened: a B3 main sequence star with $A_0 = 1.5$ needs to be at a distance of 3.8 kpc to achieve $g = 13$. The one star that has been uncovered close to IC 2581 is a candidate sub-luminous object, likely to be at a much shorter distance and unconnected to IC 2581. It can be seen in Figure 16 that $A_0 = 1.9$ for the least reddened candidate OB star in the sample.

It has been argued before by e.g. Grabelsky et al. (1988) and Dame (2007) that the Carina Arm tangent region traced in CO spans the distance range from 3 to 5 kpc. At larger distances the conical volume captured here reaches beyond the Solar Circle where declining amounts of molecular gas are detected. Taking note of these considerations, it seems likely that the high values of R_V, trending from 3.6 to 3.9, revealed by our SED fits (Figure 16) are largely a product of the dominant and increasing contribution to the total extinction from the dust column of the Carina Arm. Similarly Povich et al. (2011) found it necessary to adopt $R_V = 4$ for embedded Carina Arm objects at $l \sim 287°$. In contrast, Turner (1978) determined R_V to be 3.11±0.18 across this region, based on bright OB stars with extinctions below A_V of 2 – clearly the foreground to our sample. Indeed it seems likely that much of the extinction of the OB population spanning $A_0 \sim 2$ to $A_0 \sim 9$ accumulates within the Carina Arm. The appearance of Figure 14 indicates few detected main sequence OB stars beyond a distance modulus of 14 (6kpc).

6.2 Westerlund 2

Figures 12 and 16 tell us that a single value of R_V cannot be used to describe the extinction law of sight lines towards all objects in Wd 2. Instead we find that R_V ranges from approximately 3.5 to 4.5 within the cluster. Similar spreads in R_V within star clusters has previously been found by Fitzpatrick & Massa (2007) and highlights the importance of deriving R_V on a star-by-star basis. Hur et al. (2015) describe a hybrid extinction model with $R_V = 3.33 \pm 0.03$ to

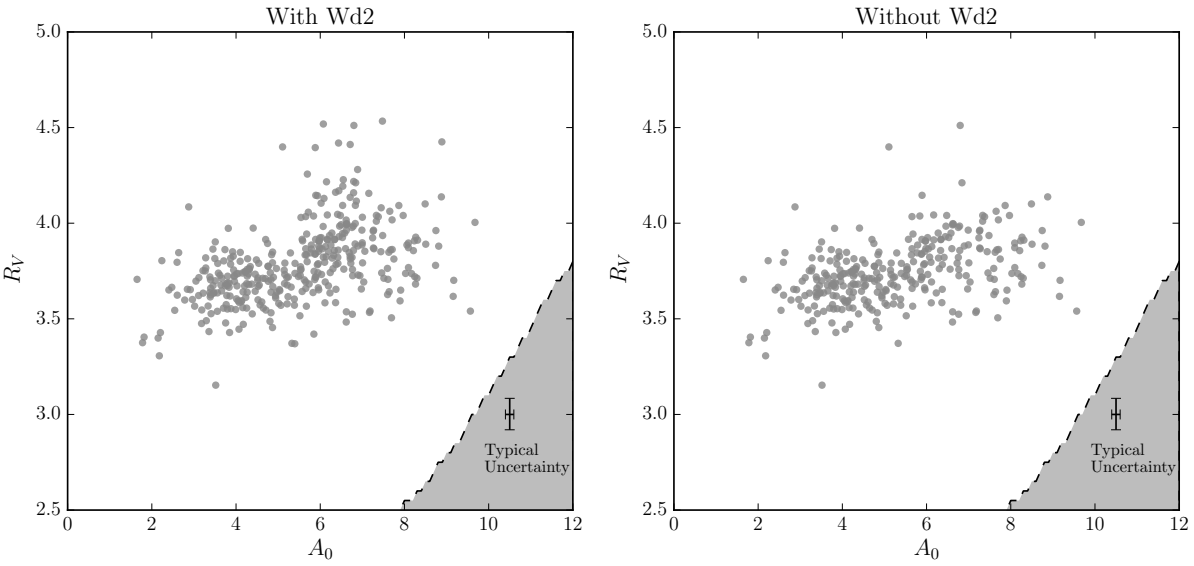

Figure 16. A_0 vs. R_V plot for the final selection with and without the objects within the 8 arcmin box surrounding Wd 2. There modest increase in R_V as a function of A_0 in either case with correlation coefficient $r = 0.47$ and $r = 0.45$ respectively. The areas shaded in grey are where we cannot detect OB stars given the survey limits.

$A_0 \sim 3$ (based on three stars), while $R_V = 4.14 \pm 0.08$ is required for stars in Wd 2. Figure 16 cautions against this clear-cut interpretation, even while our results are numerically consistent with theirs. Reality is more fractal and it is best not to place too much weight on small numbers of stars.

In Figure 12 we noticed a tight distribution in A_0 for the objects close to Wd 2 as projected on the sky. While there are no new OB star candidates in the central region of Wd 2, there are a handful of probable O stars scattered around the cluster that share its extinction. These objects are identified in Table 7. It is possible that these have been ejected from Wd 2 by dynamical interactions or after supernova explosions in binary systems (Allen & Poveda 1971; Gies & Bolton 1986). Given a derived distance of ~ 4 kpc to Wd 2, an object that is separated from the cluster by ~ 20 arcmin on the sky would have to have travelled a minimum distance of ~ 23 pc in 1–2 Myr. This would equate to a minimum (plane-of-sky) velocity of ~ 20 km/s. Given that massive stars can attain runaway velocities of up to 200 km/s through dynamical encounters between binary systems (Gvaramadze et al. 2010), it is not unreasonable to consider that these objects have been ejected recently from Wd 2. Alternatively these stars may have formed in situ within the wider star forming region on a similar time scale to the cluster. Low resolution spectroscopy of object #964 and #675 suggests their spectral types may be early as O3-O4 (Mohr-Smith et al in prep). Their positions are marked on Figure 17.

Table 7. Table containing the reddening parameters and angular separation from the centre of Wd 2 (RA 10 24 18.5 DEC -57 45 32.3 (J2000)) of new O star ($\log(T_{\rm eff}) > 4.477$) candidates near the cluster with similar reddening. See Tables 4 and 5 for the full set of data.

ID	g	A_0	Separation (arcmin)
428	17.06	6.77	36.42
511	15.23	5.53	23.87
599	15.40	6.34	23.13
675	15.58	6.60	12.60
693	15.33	6.23	12.06
728	15.27	5.65	15.49
834	16.37	6.94	12.50
964	15.01	6.11	19.67

6.3 Candidate blue supergiants and sub-luminous stars

The results from Section 5.3 suggest the presence of 5 high luminosity B stars scattered across the field. If they are early-B supergiants, their absolute visual magnitudes would be in the region of ~ -6.5 (Crowther et al. 2006). On correcting the previous main-sequence assumption, we find their derived distance moduli, μ, rise from ~ 9 to ~ 13.5, placing them amongst the general OB population that we pick out. Meylan & Maeder (1983) estimate a surface density of around 10 - 20 blue supergiants (BSGs) per kpc^2 in the Galactic Plane. Assuming that our selection spans distances from 2 - 6 kpc we are sampling a projected disk surface area of a little over 1 kpc^2; so finding 5 candidates undershoots the surface density prediction but not to the extent that it can be claimed to be inconsistent with it. Given that these candidates are affected by saturation in the i band ($i \lesssim 12$), there may one or two BSGs that have fallen into the 'poor-fit' group due to saturation in one or more bands.

We also find evidence for the presence of a population of subdwarf B (sdB) stars. The absolute magnitudes of sdB stars range from $M_V = 3 - 6$ (Stark & Wade 2003). Since these objects are ~ 6 mag fainter than their main-sequence counterparts, their distance moduli are likely to be ~ 10 as opposed to the initially derived ~ 16. This and their

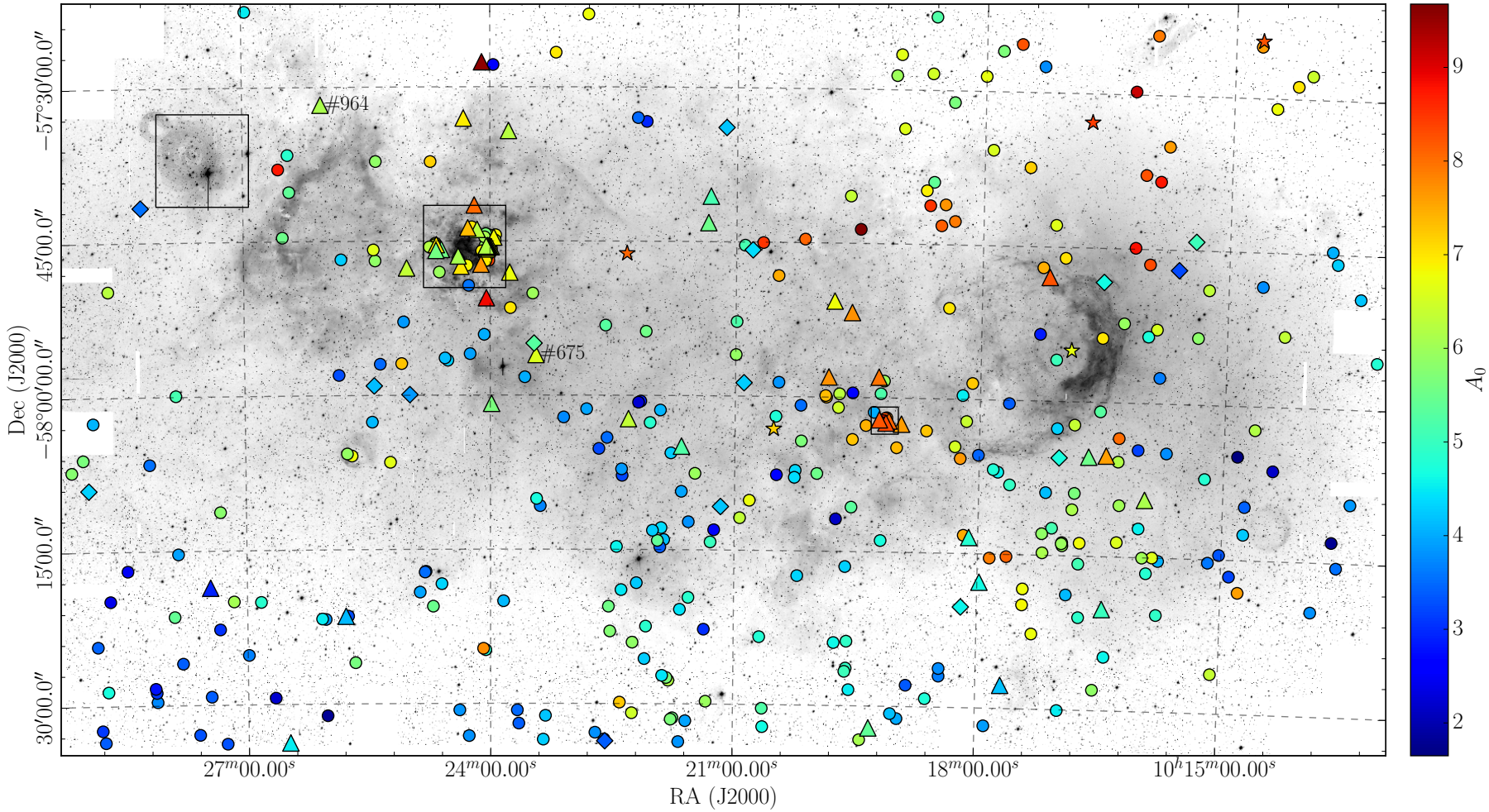

Figure 17: Known and candidate OB stars, in our selection, coloured according to their inferred reddening (A_0) and over-plotted on the high-confidence inverse VPHAS+ Hα image. The boxes pick out the known clusters IC 2581, Wd 2, and DBS2003 45 (working from east to west). The symbols used have the following interpretations: O stars with $\log(T_{\rm eff}) > 4.477$ are triangles; early B stars, $4.300 \leqslant \log(T_{\rm eff}) \leqslant 4.477$ are circles; stars and diamonds represent the blue supergiants and under-luminous objects respectively. The white space under the object near the eastern boundary is currently a region of reduced confidence in Hα (without inclusion of the adjacent field) Low resolution spectroscopy of object #964 and #675 suggests their spectral types may be early as O3-O4 (Mohr- Smith et al in prep).

© 0000 RAS, MNRAS **000**, 000–000

spatial scattering suggests that we are looking at a group of moderately reddened $A_0 \sim 4$ sdB stars in the foreground of the main OB population. We are biased to select more highly reddened sdB stars due to the 2MASS faint limit as discussed in Section 5.1.2. If this limit was not in place we would expect to find more lowly reddened sdB stars in the selection.

Although the SED-fitting we have performed has no sensitivity to surface gravities and limited sensitivity to stellar effective temperature, the fact that the Carina Arm region studied falls near the tangent has allowed us to pick out the extreme objects purely from their outlying distance moduli – relative to the near MS stars concentrated in the range $11 < \mu < 14$. While this approach works here, it is evident that in other sight-lines, where the population of OB stars may be spread more uniformly across a larger distance range, the luminosity extremes would not stand out in the same way.

7 CONCLUSIONS

In summary, we have demonstrated a method for selecting and parametrizing the reddening and basic stellar properties of OB stars uniformly across large areas of the Southern sky using VPHAS+, and NIR survey data. The selection presented here has identified more than 800 new O and B stars, of which around a half are hotter than 20000 K and 40 are probable O stars. This has been achieved by reaching down to $g = 20$ mag and represents over a factor of 15 advance relative to the small numbers of brighter candidate O and B stars (of type B2 and earlier) already known in this sight line. By bringing together VPHAS+ u, g, r, i photometry with NIR 2MASS photometry, we are able to determine both the value of the extinction, A_0, and test and select the most appropriate reddening law, as parametrised by R_V, to a high degree of accuracy: both are typically measured to better than 0.1 (magnitudes in the case of A_0). Pleasingly there are signs that the still preliminary nature of the photometric calibration of the VPHAS+ survey data blends well with the now well-established 2MASS calibration.

We set out expecting to only gain a crude impression of stellar effective temperatures (and hence distance moduli), and so it has turned out. But we have found a satisfying consistency with earlier results in our benchmark region around the much-studied cluster Westerlund 2, confirming that our methods are sound and able to e.g distinguish early O stars from late-O and early-B stars. This represents an efficient start to selection that needs to be followed up by spectroscopic confirmation and measurement of stellar parameters. With precise spectroscopic parameters in hand, the photometry can be re-used for direct and even more precise measurement of reddening laws.

We have also seen how the high resolution and wide field of view of OmegaCam can bring a wider context to the study of open clusters and OB associations, through an ability to identify potentially-related stars that have either been ejected from clusters or simply have formed – perhaps as part of a wider star-formation event – in relative isolation in the surrounding field.

In the future, we aim to roll out this method to support the complete characterisation of the massive-star population and the patterns of extinction they can reveal across the entire Southern Galactic mid-plane to distances of $\sim$ 5kpc or more. Garmany et al. (1982) were able to claim a volume-limited census to $\sim$ 2.5kpc 3 decades ago – now it should be possible to expand the effective volume by a factor of 4 or so, with the difference this time that Gaia parallaxes as they appear will bestow a confidence as to what the volume limits actually are.

ACKNOWLEDGEMENTS

This paper is based on data products from observations made with ESO Telescopes at the La Silla Paranal Observatory under programme ID 177.D-3023, as part of the VST Photometric H Survey of the Southern Galactic Plane and Bulge (VPHAS+, www.vphas.eu). Use is also made of data products from the Two Micron All Sky Survey, which is a joint project of the University of Massachusetts and the Infrared Processing and Analysis Center/California Institute of Technology, funded by the National Aeronautics and Space Administration and the National Science Foundation.

This research made use of Astropy, a community-developed core Python package for Astronomy (Astropy Collaboration et al. 2013) and TopCat (Taylor 2005).

MM-S acknowledges a studentship funded by the Science and Technology Facilities Council (STFC) of the United Kingdom (ref. ST/K502029/1). JED and GB acknowledge the support of a research grant funded by the STFC (ref. ST/J001333/1). NJW is in receipt of a fellowship funded by the Royal Astronomical Society of the United Kingdom.

REFERENCES

Allen C., Poveda A., 1971, Astrophysics and Space Science, 13, 350
Ascenso J., Alves J., Beletsky Y., Lago M. T. V. T., 2007, A&A, 466, 137
Astropy Collaboration et al., 2013, A&A, 558, A33
Bertelli G., Bressan A., Chiosi C., Fagotto F., Nasi E., 1994, A&AS, 106, 275
Bestenlehner J. M. et al., 2011, A&A, 530, L14
Bressan A., Marigo P., Girardi L., Salasnich B., Dal Cero C., Rubele S., Nanni A., 2012, MNRAS, 427, 127
Cardelli J. A., Clayton G. C., Mathis J. S., 1989, ApJ, 345, 245
Carmona A., van den Ancker M. E., Audard M., Henning T., Setiawan J., Rodmann J., 2010, A&A, 517, A67
Carraro G., Turner D., Majaess D., Baume G., 2012, ArXiv e-prints
Crowther P. A., Lennon D. J., Walborn N. R., 2006, A&A, 446, 279
Dachs J., Kiehling R., Engels D., 1988, A&A, 194, 167
Dame T. M., 2007, ApJL, 665, L163
de Bruijne J. H. J., 2012, Astrophysics and Space Science, 341, 31
de Wit W. J., Testi L., Palla F., Zinnecker H., 2005, A&A, 437, 247
Draine B. T., 2003, ARA&A, 41, 241
Drew J. E. et al., 2014, MNRAS, 440, 2036
Dutra C. M., Bica E., Soares J., Barbuy B., 2003, A&A, 400, 533
Fitzpatrick E. L., Massa D., 2007, ApJ, 663, 320

Foreman-Mackey D., Hogg D. W., Lang D., Goodman J., 2013, PASP, 125, 306
Garmany C. D., Conti P. S., Chiosi C., 1982, ApJ, 263, 777
Gies D. R., Bolton C. T., 1986, ApJS, 61, 419
Grabelsky D. A., Cohen R. S., Bronfman L., Thaddeus P., 1988, ApJ, 331, 181
Gvaramadze V. V., Gualandris A., Portegies Zwart S., 2010, in IAU Symposium, Vol. 266, IAU Symposium, de Grijs R., Lépine J. R. D., eds., pp. 413–416
Hur H., Park B.-G., Sung H., Bessell M. S., Lim B., Chun M.-Y., Sohn S. T., 2015, MNRAS, 446, 3797
Johnson H. L., Morgan W. W., 1953a, ApJ, 117, 313
Johnson H. L., Morgan W. W., 1953b, ApJ, 117, 313
Kaltcheva N. T., Golev V. K., 2012, PASP, 124, 128
Langer N., 2012, ARA&A, 50, 107
Maíz-Apellániz J., Walborn N. R., Galué H. Á., Wei L. H., 2004, ApJS, 151, 103
Martins F., Schaerer D., Hillier D. J., 2005, A&A, 436, 1049
Meylan G., Maeder A., 1983, A&A, 124, 84
Moffat A. F. J., Shara M. M., Potter M., 1991, AJ, 102, 642
Parker R. J., Goodwin S. P., 2007, MNRAS, 380, 1271
Portegies Zwart S. F., McMillan S. L. W., Gieles M., 2010, ARA&A, 48, 431
Povich M. S. et al., 2011, ApJS, 194, 6
Rahman M., Murray N., 2010, ApJ, 719, 1104
Rauw G., Manfroid J., Gosset E., Nazé Y., Sana H., De Becker M., Foellmi C., Moffat A. F. J., 2007, A&A, 463, 981
Rauw G., Sana H., Nazé Y., 2011, A&A, 535, A40
Reed B. C., 2000, AJ, 120, 314
Reed B. C., 2003, AJ, 125, 2531
Rucinski S. M., 1992, AJ, 104, 1968
Russeil D., 2003, A&A, 397, 133
Skrutskie M. F. et al., 2006, AJ, 131, 1163
Smartt S. J., 2009, ARA&A, 47, 63
Smolčić V. et al., 2004, ApJL, 615, L141
Stark A. A., Lee Y., 2005, ApJL, 619, L159
Stark M. A., Wade R. A., 2003, AJ, 126, 1455
Taylor M. B., 2005, in Astronomical Society of the Pacific Conference Series, Vol. 347, Astronomical Data Analysis Software and Systems XIV, Shopbell P., Britton M., Ebert R., eds., p. 29
Tsujimoto M. et al., 2007, ApJ, 665, 719
Turner D. G., 1978, AJ, 83, 1081
Vallée J. P., 2008, AJ, 135, 1301
Vallée J. P., 2014, AJ, 148, 5
Vargas Álvarez C. A., Kobulnicky H. A., Bradley D. R., Kannappan S. J., Norris M. A., Cool R. J., Miller B. P., 2013, AJ, 145, 125
Wenger M. et al., 2000, A&AS, 143, 9
Zhu Q., Davies B., Figer D. F., Trombley C., 2009, ApJ, 702, 929
Zorec J., Briot D., 1991, A&A, 245, 150